Wake Vortex Detection and Tracking for Aircraft Formation Flight

Ignace Ransquin*, Denis-Gabriel Caprace†, Matthieu Duponcheel‡, Philippe Chatelain§
Catholic University of Louvain, 1348, Louvain-la-Neuve, Belgium

In a fuel-efficient extended formation flight of commercial airplanes, the aerodynamic benefits depend on one's ability to surf wake vortices. This paper presents a wake vortex detection scheme based on the exploitation of the aircraft flight dynamics measurements, that effectively enables wake surfing. The study focuses on a two-aircraft formation where the follower senses, successfully locates, and tracks the wake produced by the leader over time. The proposed approach relies on an Ensemble Kalman Filter that propagates a surrogate model of the formation. The model output is here corrected within the estimator through a comparison with measurements of the full 6 degrees-of-freedom dynamics of the follower, as well as geometric characteristics of the leader. This essentially waives the need for dedicated hardware devices and only requires episodic communication between the leader and the follower. The efficiency of the novel detection strategy is demonstrated using reference data obtained from Large Eddy Simulations. It is found that the chosen combination of estimator and dynamics measurements is sufficient to detect the position of the impacting wake as long as the dynamics are accurately reproduced by the surrogate model. Additionally, it is shown that a lack of observability hinders the concurrent estimation of the wake position and strength in the presence of uncertainty. Finally, a simulation case evaluates the fuel savings that an active tracking strategy of the optimal relative positioning provides compared to a wake-independent positioning.

Nomenclature

α	=	angle of attack (°)
$\boldsymbol{\alpha}_i$	=	state additive inflation
$\mathbf{A}, \mathbf{B}, \mathbf{C}$	=	matrices of the linear state-space equation
β	=	angle of side slip (°)
$\boldsymbol{\beta}$	=	state multiplicative inflation coefficient

*Ph.D. Candidate, Institute of Mechanics, Materials and Civil Engineering (iMMC), ignace.ransquin@uclouvain.be.
†Ph.D., iMMC, denis-gabriel.caprace@uclouvain.be; present address: Brigham Young University
‡Research Engineer, Ph.D., iMMC, matthieu.duponcheel@uclouvain.be.
§Professor, iMMC, philippe.chatelain@uclouvain.be.

Æ	=	Aspect ratio
b	=	wing span (m)
Δt	=	integration time step (s)
Δt_{EnKF}	=	estimation time step (s)
$\Delta y, \Delta z$	=	leader's wake position relative to the follower's position (m)
ϵ	=	EDR
$\boldsymbol{\epsilon}_i$	=	measurement noise
$\mathbf{f}$	=	dynamic function
$\mathbf{F} = [F_x, F_y, F_z]^T$	=	aircraft resulting forces (N)
Γ	=	circulation (m^2/s)
$\mathbf{h}$	=	measurement function
$\mathbf{H}$	=	measurement matrix
$I_{.}$	=	product of inertia (kg m^2)
$\mathbf{K}$	=	Kalman gain
$\mathbf{K}_x, \mathbf{K}_{V,i}, \mathbf{K}_\beta$	=	autopilot feedback gains
m	=	mass (kg)
$\mathbf{m}$	=	propagated measurement vector
$\mathbf{M} = [M_x, M_y, M_z]^T$	=	aircraft resulting torques (kg m)
N	=	ensemble size
$(ox_i y_i z_i)$	=	inertial frame
$(ox_{ac} y_{ac} z_{ac})$	=	aircraft frame
$\mathbf{\Omega} = [p, q, r]^T$	=	roll, pitch and yaw rates (°/s)
ϕ, θ, ψ	=	angles of roll, pitch and yaw (°)
$\mathbf{P}$	=	state covariance matrix
$\mathbf{q}$	=	state vector
ρ	=	air density (kg/m^3)
$\boldsymbol{\sigma}$	=	states standard deviation vector
$\mathbf{\Sigma}$	=	inflation covariance matrix
t^*	=	dimensionless time
$\mathbf{u}_c = [\delta_{Ail}, \delta_{VTP}, \delta_{HTP}, \delta_{th}]^T$	=	control command vector
$\mathbf{V} = [U, V, W]^T$	=	airspeed (m/s)
$\mathbf{V}_K = [U_K, V_K, W_K]^T$	=	flight path velocity (m/s)

$\mathbf{V}_W$	=	wake induced velocity (m/s)
$\mathbf{V}_{\text{err}}$	=	measurement noises covariance matrix
$\mathbf{x} = [x, y, z]^T$	=	aircraft position (m)
$\mathbf{y}$	=	innovation vector
$\mathbf{z}$	=	true measurement vector

I. Introduction

Formation flying, as a bio-inspired technique, has long been known for its aerodynamic benefits [1, 2]. Early investigations conducted on a pair of aircraft (leader + follower) indeed showed that substantial fuel reduction can be achieved by the follower, both theoretically [3] and experimentally [4, 5]. Therefore, large fuel savings are at stake when it comes to the integration of formation flight into commercial aviation. This explains why the topic is intensively researched today (e.g., [6, 7]).

While migratory birds usually fly in close formation, civil aviation safety constraints permit only extended formation flight. In that case, the follower flies at several tens of wingspans downstream of the leader. Because wake vortices are energetic and long-lasting flow structures, the follower still benefits from a positive interaction with the leader's wake vortices [8, 9]. Additionally, because of the longer distance between the leader and the follower, instabilities such as meandering [10], the interactions of wakes produced by different aircraft in a formation [11], and environmental factors [12] may affect the motion of the vortices. It is therefore essential for the follower to continuously locate the wake vortices. This information can then be provided to the pilot, or an autopilot, in order to maximize the fuel savings during the flight.

Several methods allowing the follower to track the vortices have been proposed, yet not many of them were tested during actual formation flight experiments. In a first family of techniques, the position and strength of the vortices are determined from a direct measurement of the flow field [13, 14] , e.g., through a LIDAR installed on the aircraft. Today, even though ground-based measurements provide sufficiently reliable results [15], the use of such technologies still poses significant challenges for onboard wake measurements [16].

Alternative vortex detection techniques rely on indirect measurements and on estimations of the wake vortex parameters. In a first example [17], distributed pressure measurements are used on the follower wing and are processed by an estimator, essentially based on a Extended Kalman Filter (EKF), to deduce the parameters of the wake vortices currently influencing the follower. This technique showed promising results in several flight configurations, especially for deducing the position of the vortices, even though some observability issues were highlighted [18]. This technique still requires specific instrumentation to be installed aboard the aircraft though, which comes with a certain cost and design constraints. The use of conventionally available measurements has therefore been envisioned in the context of formation flight, using for instance the dynamics of the aircraft themselves feeding on peak-seeking algorithms [19, 20]. Those online techniques continuously direct the airplane towards the direction of steepest descent of a function of flight parameters (i.e., gradient descent minimization algorithm), which provides an estimation of the airplane drag or fuel consumption. A drawback to those approaches is the need for linearization of the system leading to the objective function and the absence of real-time estimation of the optimal position; the algorithm provides a direction to follow. An alternative to peak-seeking algorithms has been proposed by Hanson [21] using a fuzzy logic technique for determining and maintaining a constant lateral distance between a follower and the wake of a leader. Unlike a peak-seeking algorithms [19, 20], this fuzzy logic technique does not require the follower to track predefined trajectories (e.g., a dither signal) in order to determine the wake position.

The present work pursues the effort initiated in [22] on wake vortex detection based on data assimilation tools (i.e., Kalman filters). Two types of data were considered in that study; a first one consisted in circulation measurements along the main wing feeding the estimation of the position of an incoming wake, as suggested in [17]. A second step considered simplified aircraft dynamics. The measurements consisted solely of the dynamics of an aircraft whose motion is restricted to a translation along the vertical z_i axis, with a fixed attitude. The position, velocity, and acceleration along that axis were submitted to an idealized spring-mass system. The present study is intended to enhance the vortex detection and tracking technique by exploring the use of the full 6 degrees-of-freedom (6DOF) aircraft flight dynamics and control actions (i.e., control surface deflections) as measurements to sense the position of a wake. Such an approach is motivated by the direct availability of those measurements on current aircraft without requiring any additional hardware devices, as opposed to the above pressure-based scheme. While the use of simplified dynamics invoked in [22] showed promising results, we want to study the performance and the reliability of the methodology in realistic situations, i.e., involving full unconstrained aircraft. The 6DOF dynamics are here coupled with an autopilot in order to study the interactions between the sensing strategy and the control scheme of the follower. The full framework developed in this work enables the study of efficient strategies for the tracking of the leader's wake, which will allow the follower to maintain a fixed relative position compared to the wake vortices. To this end, and akin to [22], the estimation procedure used in this work exploits a state model of the process, itself based on a Lifting Line model that characterizes the aerodynamics of the follower. It also takes into account the nonlinear dynamics of the follower controlled by an autopilot including the influence of the leader's wake vortices. Here, the estimator itself makes use of an Ensemble Kalman Filter (EnKF), better suited to handle the nonlinearity of the process [23] than the EKF.

We employ Large Eddy Simulation (LES) in order to capture the production of the wake vortices originating from the leader, their roll-up, and the interaction with some ambient turbulence and with the follower and its wake. The aircraft are represented by several immersed lifting lines in the LES and their 6DOF dynamics are simulated in this unsteady flow flight. Every aircraft in the formation is equipped with an autopilot that commands the control surfaces and therefore the dynamics of the aircraft within the LES. Ground-truth measurements are extracted from those simulations and serve as a reference for the estimator.

Two main flight situations are established and are thoroughly investigated in this work. The first one explores the ability for a follower flying on a predefined trajectory to use measurements obtained from its dynamics in order to estimate the position of the wake produced by a static or a moving leader, whose geometry (i.e., mass and dimensions) is known. The second one investigates the situation where the follower detects the position of the wake of a moving leader and concurrently follows a target position relative to that estimated wake location as a way to constantly benefit from the wake upwash. In the first case, the trajectory of the follower is independent of the dynamics of the leader, whereas in the second situation, the trajectory of the follower relies on the estimation of the wake location and is therefore highly influenced by the leader's behavior. The performances of the estimator are therefore impacted, as well as the flying performances of the follower (i.e., reduction in thrust command). These simulations suggest that the use of the follower dynamics is sufficient to determine the position of an impacting wake. We show the performance of the estimator for different flight configurations. At the same time, we also investigate the ability of the estimator to determine the intensity of the wake of a leader, in addition to determining its position. Indeed, while the geometry of a leader does not change during a given flight, its mass decreases, inducing a change in its wake intensity. Finally, our results highlight the known observability issues [17, 18] that arise from the multiplicative compensation between the wake intensity and the lateral position when dealing with more challenging configurations (i.e., a moving wake or strong turbulence).

The contributions of this work lie in the application of an EnKF that processes measurements of a follower's dynamics in order to estimate and track the position of a leader's wake and in the validation of the sensing and control scheme in a high-fidelity flight environment based on LES. This article is structured as follows. Section II introduces the complete detection architecture. The latter is built in a high-fidelity flight environment in which we simulate various configurations of formation flight and the estimator itself that propagates a low-fidelity state model of those configurations. Section III validates the state model by comparing the 6DOF dynamics of an aircraft produced by both the state model and the high-fidelity flow environment. The performance of the autopilot are also highlighted. Finally Section IV assesses the estimation quality of the wake position for the two considered flight situations. We also evaluate the ability of the estimator to determine the intensity of the wake, in addition to its position. Considerations of the observability of the dynamics based estimation strategy are therefore discussed. Concluding remarks are made in Section V.

II. Design of the Wake Detection and Tracking Strategy

In designing a reliable wake detection and tracking approach, instead of considering actual flight tests, we will use a high-fidelity representation of the flight environment of a two-aircraft formation. Our simulated flight environment represents reality and will produce the reference measurements that feed the estimator. The estimator makes use of an EnKF in order to process those measurement and to estimate the characteristics of the wake influencing the follower. This is done through the exploitation of a state model representation of the two-aircraft formation, called the surrogate model as opposed to the high-fidelity flight environment. Fig. 1 is a schematic representation of the complete architecture. The latter combines the simulated flight environment, the EnKF, the surrogate model, and a filtering tool used to provide a smooth target to the autopilot.

The current section introduces the high-fidelity flight environment in Section II.A. Section II.B presents the equations of the EnKF, which relies on the surrogate model described in Section II.C. The filtering procedure is described in Section IV.B.

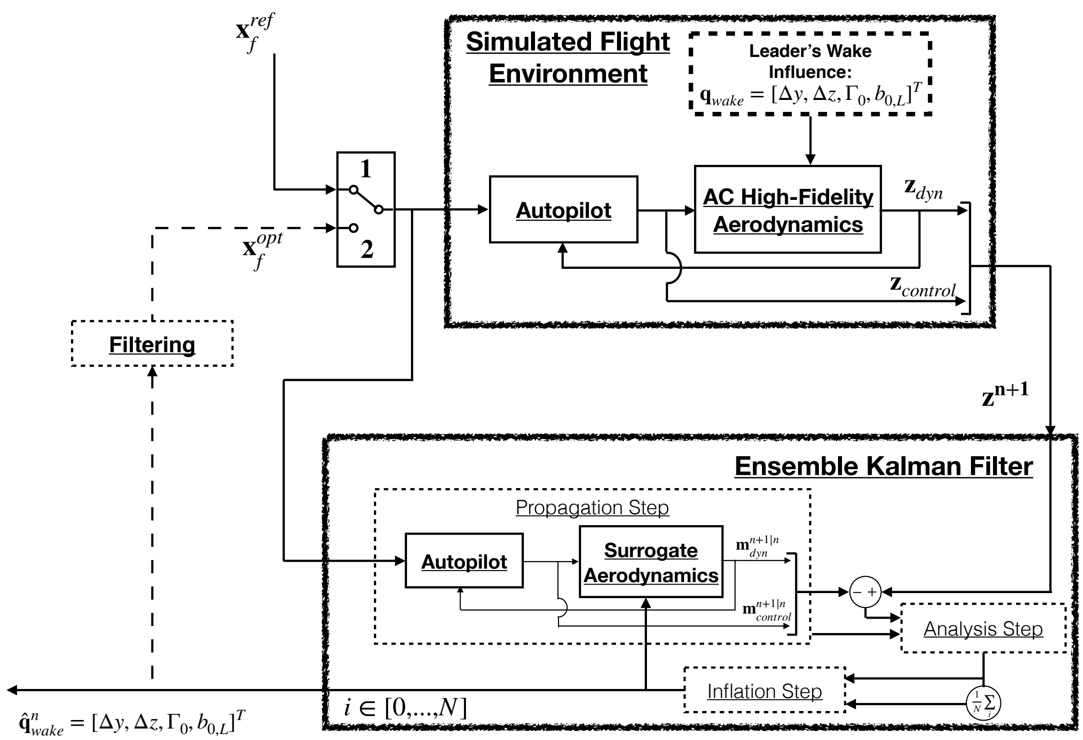

Figure 1 Block diagram of the tracking strategy including the simulated flight environment, the estimator, and a filtering tool to provide a smooth target.

A. Simulated flight environment

A sensing strategy is evaluated by its ability to perform in an environment as close as possible to real flight conditions, which means in this work the nonlinear and unsteady environment produced by the wake of a leader and a follower flying in extended formation. The Vortex Particle-Mesh method (VPM) [24] is used to simulate the unsteady wake developed by this system of two aircraft. The VPM method exploits the vorticity-velocity formulation of the Navier-Stokes equations expressed in a hybrid Lagrangian-Eulerian framework [25] in order to solve unbounded incompressible flows. This Large Eddy Simulation approach was proven very efficient for the simulation of complex wake flows emanating from wings [26], wind turbines [27, 28] and helicopters [29] over long distance, which is thus well suited for this study.

In the present application, the leader and the follower aircraft are of the same type, have identical parameters and are each represented by three straight Immersed Lifting Lines [30]: one for the wing, one for the Horizontal Tail Plane (HTP), and one for the Vertical Tail Plane (VTP). Each lifting line uses the local flow velocity and tabulated airfoil data to determine the bound vorticity and the vorticity that must be shed in the wake as a signature of lift. This vorticity is then advected with the flow, eventually interacting with ambient turbulence or nearby wakes. The ensuing wake roll-up process is accurately captured, even at high Reynolds numbers, as the dissipation of the method is well controlled, thanks to its Lagrangian character and the use of a regularized variational subgrid-scale model [31].

Within the flow simulation, the motion of each aircraft is computed through the time-integration of their respective 6DOF equations of motion. Furthermore, control surfaces at each lifting surface (i.e., ailerons, rudder and elevator) are also taken into account as a local modification of the polar in order to model the corresponding change in aerodynamic loads. The geometrical characteristics of each aircraft and, in particular, the geometrical incidences of the wing and the elevator, are initially configured in order to cancel the aerodynamic loads undergone by an isolated aircraft in a trimmed level flight: the generated lift balances the aircraft weight and the pitching moment is canceled. Then, depending on the flight configuration, an autopilot generates inputs for the control surfaces in order to control the trajectory of the aircraft or to balance the efforts arising from the surrounding environment (e.g., the rolling moment induced by the wake of the leader on the follower).

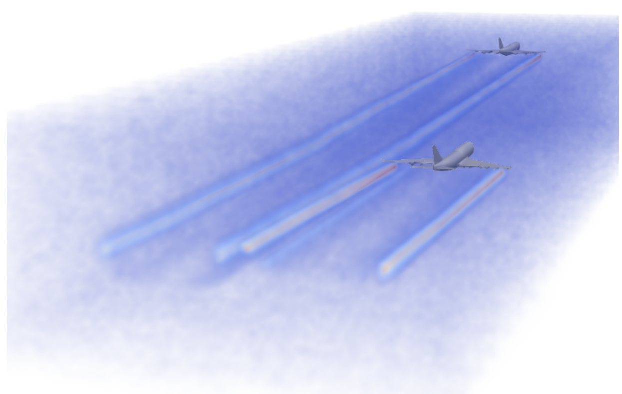

Figure 2 Volume rendering of the vorticity in the wake of two-aircraft formation, with ambient turbulence. Immersed lifting lines are displayed as realistic 3D aircraft.

In this work, ambient turbulence is added to the simulation to reproduce as closely as possible actual flight and wake conditions. From the estimator point of view, this corresponds to a natural source of process noise in the estimation routine, as the turbulence is not modeled in the surrogate model described in Section II.C. Synthetic turbulence, reproducing the spectrum of Homogenous Isotropic Turbulence (HIT), and generated using the Mann algorithm [32], is smoothly injected at the inlet of the computational domain. This affects the wake generation mechanism and may trigger instabilities. Fig. 2 is a visual representation of the turbulent environment in which the two-aircraft formation evolves, and in which the wake detection strategy performs.

B. Estimator and Kalman filtering

This work relies on the discrete-time Kalman filter framework to estimate the characteristics of the leader's wake vortices. With regard to the estimator, those characteristics are represented by a wake state vector $\mathbf{q}_{\text{wake}}$. Associated to the follower's dynamics state vector $\mathbf{q}_{\text{dyn}}$, they form the state vector $\mathbf{q}$ that is propagated by the estimator over time, using to the surrogate model. The propagation step produces the predicted measurement vector $\mathbf{m}$, which is compared to the true measurement vector $\mathbf{z}$ in order to produce an updated estimated state during the analysis step. The state vector $\mathbf{q}$, the measurements $\mathbf{z}$ (or $\mathbf{m}$), and the surrogate model are described in detail in Section II.C. We focus on the description of the filtering methodology here.

The nonlinearity of the system under investigation associated to the complex flow environment makes the classical Kalman Filter (KF) for linear systems inadequate. The Extended Kalman Filter (EKF), which requires the linearization of the system about the current state, was also proven unsuccessful in some configurations when applied to the current problem [17]. Biases on the solution, or even diverging behaviors were observed, and are likely to be related to the observability structure of the wake, or to the nonlinearity through an uncontrolled growth of the error covariance. To overcome these issues, we here use the Ensemble Kalman Filter (EnKF) [33] with implicit linearized formulation for the measurements [34], schematically described in Fig. 3 and in the continuity of the work carried out in [22].

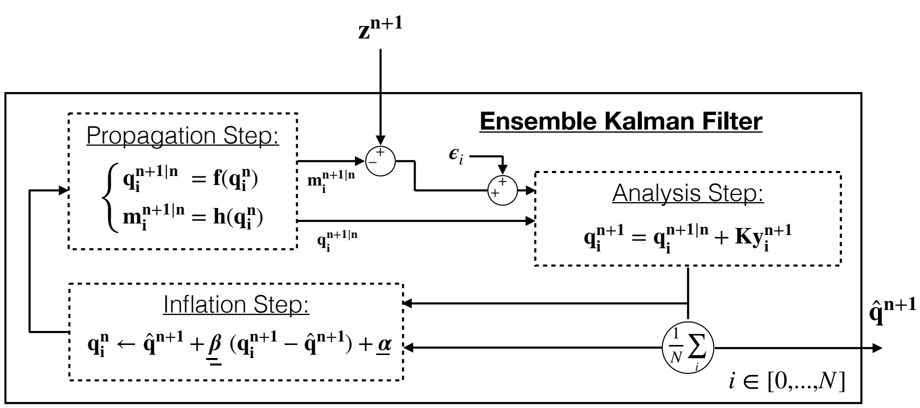

Figure 3 Ensemble Kalman Filter scheme

The EnKF uses a Monte Carlo approach to propagate the probability density function (PDF) of the states through the system, meaning that the state vector $\mathbf{q}$ is represented by a discrete ensemble of size N. Then, approximate statistics of the propagated distribution can be computed from the ensemble and the resulting mean and covariance matrices are used as in a classical KF. An analysis step and a covariance inflation step follow the propagation step every time the filtered state is iterated.

The propagation step consists in the forward time evolution of each member $\mathbf{q}_i^n$ of the ensemble from iteration n to

$n + 1$ through the surrogate model of the flight environment

$$\begin{cases} \mathbf{q}_i^{n+1|n} = \mathbf{f}(\mathbf{q}_i^n) \\ \mathbf{m}_i^{n+1|n} = \mathbf{h}(\mathbf{q}_i^n), \end{cases} \tag{1}$$

where $(.)^{n+1|n}$ denotes the propagation of the model without any measurements incorporated in the estimation process, $\mathbf{m}$ is the measurement vector, and $\mathbf{f}$ and $\mathbf{h}$ are non-linear functions describing the dynamics of the state model. Unlike the classic definition of the KF, note that the state model does not include any process noise $\mathbf{w}$. We can now estimate the *a priori* state mean and covariance based on the propagated ensemble, i.e.,:

$$\hat{\mathbf{q}}^{n+1|n} = \frac{1}{N} \sum_{i=1}^{N} \mathbf{q}_i^{n+1|n}, \tag{2}$$

$$\mathbf{P}^{n+1|n} = \frac{1}{N-1} \sum_{i=1}^{N} (\mathbf{q}_i^{n+1|n} - \hat{\mathbf{q}}^{n+1|n})(\mathbf{q}_i^{n+1|n} - \hat{\mathbf{q}}^{n+1|n})^T. \tag{3}$$

The innovation step is performed by comparing the true measurements $\mathbf{z}^{n+1}$, i.e. those obtained from the high-fidelity flight environment at the current assimilation time, and the measurement vector $\mathbf{m}_i^{n+1|n}$ of each element of the ensemble,

$$\mathbf{y}_i^{n+1} = (\mathbf{z}^{n+1} + \boldsymbol{\epsilon}_i) - \mathbf{m}_i^{n+1|n}, \tag{4}$$

where the random vector $\boldsymbol{\epsilon}_i \sim \mathcal{N}(0, \mathbf{V}_{\text{err}})$ is the additive measurement noise. Unlike the process noise, the measurement noise is thus explicitly introduced within the simulations and then allows the innovation step to compare independent random vectors. Indeed, we cannot use the same measurement $\mathbf{z}^{n+1}$ for all the ensemble members, as Burgers et al. [35] found that doing so in an ensemble no longer reflects the fact that $\mathbf{z}^{n+1}$ is drawn from a random variable, and will introduce spurious correlations in the ensemble covariance [36]. The measurement noise has a very specific physical meaning, as it is directly related to the precision of sensors used in a real application. This has to be kept in mind when tuning the values of the measurement noise covariance matrix $\mathbf{V}_{\text{err}}$.

Then, the analysis step starts with the use of the sample covariance to compute the Kalman gains $\mathbf{K}^{n+1}$, using the standard definition [33] without any further modification, i.e.,

$$\mathbf{K}^{n+1} = \mathbf{P}^{n+1|n}(\mathbf{H}^{n+1|n})^T \left(\mathbf{V}_{\text{err}}^{n+1} + \mathbf{H}^{n+1|n}\mathbf{P}^{n+1|n}(\mathbf{H}^{n+1|n})^T\right)^{-1}, \tag{5}$$

where $\mathbf{H}^{n+1|n}$ is the measurement matrix obtained in the frame of an implicit linearized formulation [37]. In practice, it means that the measurement matrix $\mathbf{H}^{n+1|n}$ is not directly computed. Instead, an approximation of the products $\mathbf{P}^{n+1|n}(\mathbf{H}^{n+1|n})^T$ and $\mathbf{H}^{n+1|n}\mathbf{P}^{n+1|n}(\mathbf{H}^{n+1|n})^T$ can be computed given the prior ensemble [34]. All the members of the ensemble thus share the same Kalman gain, but have their own innovation. Indeed, each member of the ensemble is individually updated using the Kalman gain in its classical form,

$$\mathbf{q}_i^{n+1} = \mathbf{q}_i^{n+1|n} + \mathbf{K}^{n+1}\mathbf{y}_i^{n+1}. \tag{6}$$

We deduce the updated *a posteriori* state and covariance matrix of the system by taking the mean $\hat{\mathbf{q}}^{n+1}$ and covariance $\mathbf{P}^{n+1}$ of the updated ensemble members:

$$\hat{\mathbf{q}}^{n+1} = \frac{1}{N}\sum_{i=1}^{N}\mathbf{q}_i^{n+1}, \tag{7}$$

$$\mathbf{P}^{n+1} = \frac{1}{N-1}\sum_{i=1}^{N}(\mathbf{q}_i^{n+1} - \hat{\mathbf{q}}^{n+1})(\mathbf{q}_i^{n+1} - \hat{\mathbf{q}}^{n+1})^T. \tag{8}$$

Similarly to the classical KF, the EnKF minimizes the covariance of the estimated state distribution $\mathbf{P}^{n+1}$. However, as opposed to a KF, the covariance of the states is not bounded from below by the covariance of the state disturbance. Indeed, the EnKF does not process any process noise when it computes the covariance, as already mentioned. As described in [36], this process noise is explicitly added to the ensemble members in the EnKF, because of its Monte Carlo formulation of the KF. Therefore, the progressive decrease of the ensemble covariance $\mathbf{P}^{n+1|n}$, despite a non-zero measurement covariance $\mathbf{V}$, would yield negligible Kalman gain $\mathbf{K}^{n+1}$. Hence, the innovation vector would be ignored in Eq. (6), rendering the filter totally ineffective. Covariance inflation is thus implemented by altering the state ensemble of each vector. The Relaxation To Prior Spread (RTPS) technique [38], as well as additive inflation, lead to

$$\mathbf{q}_i^{n} \leftarrow \hat{\mathbf{q}}^{n+1} + \boldsymbol{\beta}(\mathbf{q}_i^{n+1} - \hat{\mathbf{q}}^{n+1}) + \boldsymbol{\alpha}_i, \tag{9}$$

with $\boldsymbol{\beta} = 1 + \theta\left(\frac{\boldsymbol{\sigma}^b - \boldsymbol{\sigma}^a}{\boldsymbol{\sigma}^a}\right)$, where $\boldsymbol{\sigma}^a$ and $\boldsymbol{\sigma}^b$ are the standard deviation of the prior $\mathbf{q}_i^{n+1|n}$ and of the posterior $\mathbf{q}_i^{n+1}$ states, respectively, and $\theta = 0.7$. $\boldsymbol{\alpha}_i \sim \mathcal{N}(0, \boldsymbol{\Sigma})$ is the small random additive inflation. The multiplicative inflation $\boldsymbol{\beta}_i(\mathbf{q}_i^{n+1} - \hat{\mathbf{q}}^{n+1})$ is used to spread the ensemble around the state mean while the additive inflation $\boldsymbol{\alpha}_i$ is used as a representation of the process noise that is missing in the surrogate model Eq. (1). More details on the theoretical background to the EnKF can be found in [33]. In addition to its ease of implementation, this approach generally enables the filtering of systems with a very large number of degrees of freedom up to several millions [37]. The EnKF processes measurements provided by those large systems thanks to models involving a reduced number of states (e.g., of the order of a hundred in [37]) and therefore estimates those systems at a more reasonable cost. In this work, the states are the ones involved in the equations of motion of an aircraft subjected to the influence of an external wake, i.e., 12 for the follower's dynamics and 4 for the leader's wake dynamics. We also use the EnKF to exploit its ability to handle nonlinear processes, which is required for an accurate estimation of the wake characteristics as highlighted in [17] and [22].

C. Surrogate model

We adopt a state model representation for the process formally described by $\mathbf{f}$ and $\mathbf{h}$ in Section II.B. This model has to be computationally affordable as it is evaluated at every iteration of the estimation process, and for each member of the ensemble. In order to ensure an accurate estimation of the relative position of the follower with respect to the instantaneous position of the leader's wake, the measurements $\boldsymbol{m}$ produced by the surrogate model have to be similar to the measurements z provided by the high fidelity flight-environment for identical flight configurations. Since the detection strategy relies on the follower dynamics, the surrogate model has to correctly reproduce the aerodynamic loads undergone by the follower in those configurations. The states of our two-aircraft formation model consist of the characteristics of the leader's wake $\mathbf{q}_{\text{wake}}$ and the dynamics of the follower $\mathbf{q}_{\text{dyn}}$. The former are described in Section II.C.1, where we present the aerodynamics of the surrogate model. The latter are introduced in Section II.C.2, where we describe the 6DOF equations of motion of the aircraft. Finally, Section II.C.3 details the structure of the autopilot that controls the motion of the aircraft. The measurements $\mathbf{m}$ (or $\mathbf{z}$) processed by the estimator are also described throughout those sections.

1. Aerodynamics

The Prandtl Lifting Line (PLL) theory is implemented as the simplified aerodynamic model of the high-fidelity flight environment for the estimator. It was chosen for its relatively high degree of fidelity while remaining computationally affordable. Indeed, akin to the high-fidelity flight environment described in Section II.A, the lines use flow velocities to determine the aerodynamic loads on each one of lifting surfaces. However, the wake is much simplified as the propagation and roll-up of the unsteady wake resulting from the movement of the aircraft is not considered though. We show in Section III that this model guarantees similar 6DOF dynamics to the ones of the flight environment, but at a computational cost that is compatible with a real time application.

As depicted in Fig. 4, the follower aircraft is located at the inertial position $\mathbf{x}_F = [x_F, y_F, z_F]_i^T$ and is represented by three straight lifting lines similar to those used in VPM simulations and described in Section II.A. The tail, made of the VTP and the HTP, is located downstream of the wing at a distance $\boldsymbol{d}_t$ from the center of the wing. Following the PLL theory, the wake of an aircraft is made of one flat vortex sheet produced by the wing and the two perpendicular vortex sheets produced by the tail due to the HTP and the VTP (see Fig. 4). All those vortex sheets are assumed to go straight to infinity, whereas the high-fidelity flight environment models the roll-up of the sheet into two counter-rotating vortices. The downwash induced by the wing and its wake on the tail is taken into account in the evaluation of the intensity of the vortex sheets shed by the tail. However, this downwash is evaluated as that of the equivalent horseshoe vortex of intensity $\Gamma_{0,w}$. This provides a sufficiently accurate yet computationally cheap evaluation of the dynamics of the aircraft

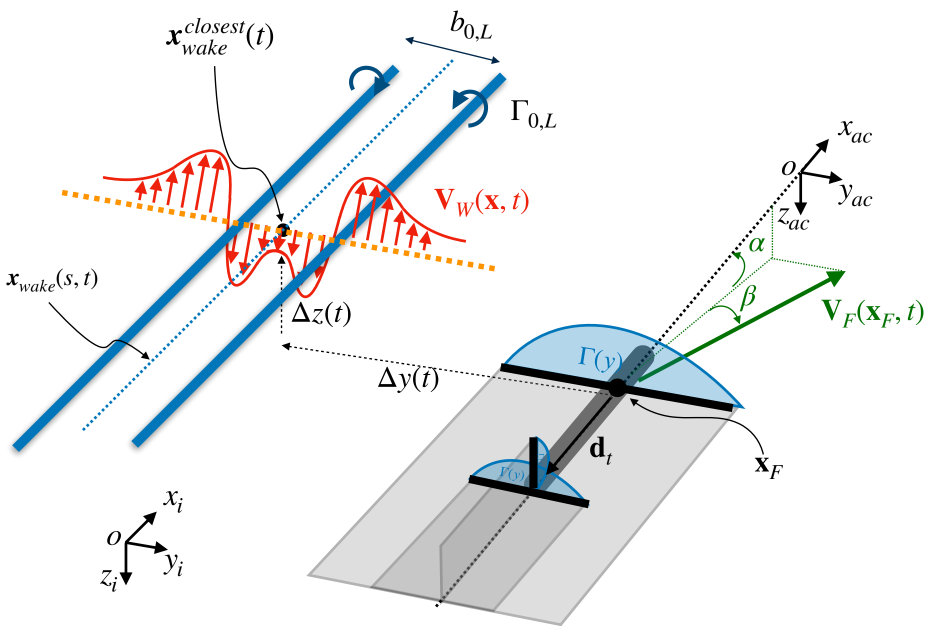

Figure 4 Aerodynamic model of the follower with three lifting lines (black), their wake (light grey) and their circulation distributions (light blue). The velocities induced by the leader's two vortices are depicted in red.

over time, as the loads on the tail considerably influence the longitudinal and lateral behavior of an aircraft.

The wake of the leader is modeled as two straight counter-rotating vortex tubes of circulation $\Gamma_{0,L}$ and spacing $b_{0,L}$. Those two parameters are directly related to the mass m and the geometry of the leader, i.e., its span b. For an aircraft in steady flight, we have

$$m_L g = \rho V_\infty \Gamma_{0,L} b_{0,L}, \tag{10}$$

where g is the gravity constant, ρ the ambient air density, V_∞ the cruise speed of the leader, and $b_{0,L} = b_L \frac{\pi}{4}$ for an elliptic span loading. Even if approximated, the information $\Gamma_{0,L}$ and $b_{0,L}$ yields the correct order of magnitude. While Flanzer et al. [7] use the Automatic Dependent Surveillance-Broadcast (ADS-B) for an experimental formation flight application in order to determine the wind speed, we hypothesis a reasonable extension of the ADS-B, namely the episodical broadcast of minimal leader's properties, in particular its mass m. In this work, this hypothesis translates in our assumption that the leader's properties are initially known, and vary little within the time scales considered. The vortices are aligned with the inertial x_i axis (which is parallel to the ground), and are regularized using a low-order algebraic wake vortex model (also called the Burnham-Hallock model), with a core radius $r_c/b = 0.05$ [39]. We use the quantities $[\Delta y, \Delta z]_i$ to represent the relative distance between the follower and the position of the leader's wake. Let us define $\boldsymbol{x}_{\text{wake}}(s,t)$ as the function describing the position of the centerline of the leader's wake with respect to time and the curvilinear coordinate s. We also define the time varying position of the wake $\boldsymbol{x}_{\text{wake}}^{\text{closest}}(t)$ as the point belonging to the centerline $\boldsymbol{x}_{\text{wake}}(s,t)$ such that the distance to the follower position is minimal, i.e.,

$$\boldsymbol{x}_{\text{wake}}^{\text{closest}}(t) = \arg\min_{s} \left(\|\boldsymbol{x}_{\text{wake}}(s,t) - \boldsymbol{x}_F(t)\| \right). \tag{11}$$

Δy and Δz are the vertical and lateral components of the vector $\boldsymbol{x}_{\text{wake}}^{\text{closest}} - \boldsymbol{x}_F$.They therefore measure the relative distance of the follower to the wake and not to the position of the leader. Unlike this relative distance, which varies depending on external factors [12] and on the trajectories of the leader and of the follower, the circulation $\Gamma_{0,L}$ and spacing $b_{0,L}$ are assumed constant. Indeed, they vary with the mass of the leader, which decreases slowly compared to the detection and tracking time scale.

The wake-induced velocities $\mathbf{V}_W(\mathbf{x},t)$ on the follower's wing, VTP and HTP depend on the spanwise location as well as on the follower's angular position relative to the leader's wake. The complete dynamics of the follower, combined with the induced velocities, lead to the airspeed vector $\mathbf{V}_F(\mathbf{x}_F,t)$ of the follower. When measured at the center of mass of the follower, this relative air velocity vector enables the computation of the related aerodynamic angles α and β, i.e., the angle of attack and the angle of slip, respectively.

Using the Prandtl lifting line theory, one computes the circulation distribution along all the lifting lines, through solving the integro-differential equation that relates the circulation with the airspeed along the lines, i.e., the sum of the velocities induced by the follower's movement, the leader's wake, and the lifting lines themselves. This equation arises from the Kutta-Joukowski theorem [40] [41] and from the definition of the sectional lift slope a_0. The equations to be solved are presented in [42], and the solution is the circulation distributions of the follower's wing, VTP and HTP, i.e., Γ_w, Γ_{VTP} and Γ_{HTP}, respectively. While the wing can be resolved independently from the tail (as we neglect the small influence of the latter on the former), the latter requires the resolution of a single coupled system, where the distribution of circulation on the VTP and the HTP are computed within the same system. The wing distribution is resolved first and the resulting shed vortex sheet is assumed to be rolled-up instantaneously into a vortex pair. This term then generates induced velocities on each the VTP and HTP. In practice, the resolution of these lifting lines entails the inversion of two linear systems, i.e., one for the wing, the other for the tail. The inverse matrices can be stored and reused at every time step, which makes the resolution computationally inexpensive.

The lift and induced drag forces as well as the rolling and yawing moments are readily deduced from the circulation distributions. Applying the vortex lifting law to a differential segment of the lifting line, we have

$$\begin{cases} d\boldsymbol{F} &= \rho\Gamma \boldsymbol{V} \times d\boldsymbol{l} \\ d\boldsymbol{M} &= \rho\Gamma \boldsymbol{x} \times (\boldsymbol{V} \times d\boldsymbol{l}), \end{cases} \tag{12}$$

with $\boldsymbol{V}$ the airspeed, Γ the circulation along the segment $d\boldsymbol{l}$ of the lifting line located in $\boldsymbol{x}$, and $\times$ the cross product. We also use polars in order to take into account the lifting surfaces parasitic drag and pitching moment. For instance, we have the contribution $\mathbf{F}_w = [F_{x,w}, F_{y,w}, F_{z,w}]_{ac}^T$ and $\mathbf{M}_w = [M_{x,w}, M_{y,w}, M_{z,w}]_{ac}^T$ from the wing that is aligned with the y_{ac} axis in the aircraft frame $(ox_{ac}y_{ac}z_{ac})$ in Fig. 4, i.e.,

$$\begin{cases} F_{x,w} &= \rho \int_{\frac{-b_w}{2}}^{\frac{b_w}{2}} \left[\Gamma_w U_w \left(\frac{W_w}{U_w} \right) - \frac{1}{2} c U_w^2 C_{d,0} \right] dy \\ F_{y,w} &= 0 \\ F_{z,w} &= -\rho \int_{\frac{-b_w}{2}}^{\frac{b_w}{2}} \Gamma_w U_w dy \\ M_{x,w} &= \rho \int_{\frac{-b_w}{2}}^{\frac{b_w}{2}} \Gamma_w U_w y dy \\ M_{y,w} &= \rho \int_{\frac{-b_w}{2}}^{\frac{b_w}{2}} \frac{1}{2} c^2 U_w^2 C_{m,0} dy \\ M_{z,w} &= -\rho \int_{\frac{-b_w}{2}}^{\frac{b_w}{2}} \left[\Gamma_w U_w \left[\frac{W_w}{U_w} \right] y dy + \int_{\frac{-b_w}{2}}^{\frac{b_w}{2}} \frac{1}{2} c U_w^2 C_{d,0} y \right] dy, \end{cases} \tag{13}$$

where c and Γ_w are the chord and circulation distributions, and $C_{d,0}$ and $C_{m,0}$ are the parasitic drag and pitching moment polars. $\mathbf{V}_w(\boldsymbol{x}_w, t) = \mathbf{V}_{K,F}(t) + \boldsymbol{\Omega}_F \times \boldsymbol{x}_w - \boldsymbol{V}_W(\boldsymbol{x}_w, t) = [U_w, V_w, W_w]_{ac}^T$ is the airspeed at each section $\boldsymbol{x}_w$ along the wing of the follower, with $\boldsymbol{\Omega}_F$ the angular velocity of the follower. The total aircraft forces $\mathbf{F}_F$ and moment $\mathbf{M}_F$ are then computed at the center of mass of the aircraft by gathering the contributions from the wing, VTP, and HTP as well as the gravity force and the thrust applied by the engine.

In summary, for the aerodynamic part of the model, the variables characterizing the wake of the leader are

$$\boldsymbol{q}_{\text{wake}} = \left[\Delta y, \Delta z, \Gamma_{0,L}, b_{0,L} \right]^T .$$

Those variables are the unknown states of the complete system, as the dynamics of those variables is *a priori* unknown. The goal of the estimator is to determine the value of those states over time.

The relative positions $(\Delta y, \Delta z)$ cannot be directly measured over time; the objective of our technique is precisely to determine them using aircraft dynamics measurements. Their dynamics are governed by Eq. (11). The spacing $b_{0,L}$ is constant supplied to the EnKF as a measurement in the vectors $\mathbf{z}$ and $\mathbf{m}$. Indeed, aircraft flying in extended formation flight configurations are assumed to know the geometrical properties of eachother. Finally, regarding the wake intensity $\Gamma_{0,L}$, we initially assume that it is constant and available in the measurement vectors $\mathbf{z}$ and $\mathbf{m}$ over time. This assumption permits us to evaluate the ability of the detection strategy to determine the position of a wake of a leader. Section IV assesses the ability of the EnKF to deal with the state $\Gamma_{0,L}$ unmeasured and thus *a priori* unknown over time in order to test the robustness of the filter (i.e. the measurement vectors $\mathbf{z}$ and $\mathbf{m}$ will not include $\Gamma_{0,L}$). Therefore, for the aerodynamic part of the model, the list of available measurements is

$$\mathbf{m}_{\text{angle}} = [\alpha, \beta]^T, \quad (14) \qquad \mathbf{m}_{\text{wake}} = \left[\Gamma_{0,L}, b_{0,L}\right]^T, \quad (15)$$

with the measurement $\Gamma_{0,L}$ being included in the wake measurement only.

2. Flight Dynamics

The flight mechanic model uses the forces and moments computed by the aerodynamic model and integrates the aircraft 6DOF equations of motion over time. This allows the prediction of the position, attitude, and velocity of the follower over one time step of the filter. As we want to impose the position of a follower, compared to the position of the wake of leader, we describe the motion of the aircraft in the inertial frame $(ox_i y_i z_i)$. The position $\mathbf{x}_F = [x_F, y_F, z_F]_i^T$ and flight path velocity $\mathbf{V}_{K,F} = [U_{K,F}, V_{K,F}, W_{K,F}]_i^T$ are computed using the total aerodynamical forces, gravity forces, and thrust forces leading to the resultant force vector $\mathbf{F}_F = [F_x, F_y, F_z]_i^T$.

The angular position $[\phi, \theta, \psi]^T$ consists of three rotations with ϕ the bank, θ the pitch, and ψ the azimuth, i.e., the three Tait-Bryan angles. The three corresponding rotations describe the transformation from the inertial frame to the aircraft frame and are integrated over time using the angular body rates $[p, q, r]^T$. Those body rates evolve over time depending on the aerodynamic moments in the aircraft frame $(ox_{ac} y_{ac} z_{ac})$, $\boldsymbol{M}_F = [M_x, M_y, M_z]_{ac}^T$. Due to the symmetry of the aircraft with respect to the (xz) plane, the products of inertia $I_{xy} = I_{yz} = 0$. We also assume that the aircraft body axes are aligned to be principal inertia axes. In this special case, the remaining product of inertia I_{xz} is also zero (see [43]). The equations of motion for the three translations and the three rotations are

$$m\dot{\boldsymbol{V}}_{K,F} = \mathbf{F}_F \quad (16)$$

$$\dot{\boldsymbol{x}}_F = \mathbf{V}_{K,F} \quad (17)$$

$$\begin{cases} I_x\dot{p} - (I_y - I_z)qr = M_x \\ I_y\dot{q} + (I_x - I_z)pr = M_y \\ I_z\dot{r} - (I_x - I_y)pq = M_z \end{cases} \quad (18)$$

$$\begin{bmatrix} \dot{\phi} \\ \dot{\theta} \\ \dot{\psi} \end{bmatrix} = \begin{bmatrix} 1 & \sin\phi\tan\theta & \cos\phi\tan\theta \\ 0 & \cos\phi & -\sin\phi \\ 0 & \sin\phi\sec\theta & \cos\phi\sec\theta \end{bmatrix} \begin{bmatrix} p \\ q \\ r \end{bmatrix} \quad (19)$$

with m the mass of the aircraft.

The forces and moments depend on the states of the system and are therefore strongly coupled to the aerodynamic model. The latter also needs the position and velocity of the aircraft in order to compute the forces and moments. Note that the same equations of motion are used to compute the dynamics of each airplane when using the VPM framework presented in Section II.A. In that case, we recall that, crucially, the aerodynamic loads are obtained using the VPM tool and not the surrogate model. This difference will be invoked to explain the discrepancies observed in Section III.

Finally, with the flight dynamics model, the state vector can be augmented with

$$\mathbf{q}_{\text{dyn}} = [x_F, y_F, z_F, U_F, V_F, W_F, \phi, \theta, \psi, p, q, r]^T, \quad (20)$$

and this turns readily into the additional available measurements

$$\mathbf{m}_{\rm dyn} = [x_F, y_F, z_F, U_F, V_F, W_F, \phi, \theta, \psi, p, q, r]^T. \tag{21}$$

3. Aircraft autopilot

The autopilot designed here will be used to pursue two different objectives. The first mode, hereafter referred to as *position hold*, enables the follower to maintain a fixed desired position $\boldsymbol{x}_F^{ref}$. In the second mode, the autopilot actively targets a constant relative position $\boldsymbol{x}_F^{opt}$ compared to the wake (i.e., the output of the estimator). The latter mode is called *wake tracking*. Acting on the complete 6DOF dynamics of the aircraft, the autopilot commands the control inputs of the aircraft in order to maintain a fixed position, or to follow the moving target, i.e., *position hold* mode (switch 1 in Fig. 1) or *wake tracking* mode, respectively (switch 2 in Fig. 1).

While the state model used to represent the aerodynamic forces is nonlinear (see Section II.C.1), the design of the autopilot and mostly the computation of the feedback gains was performed based on a linear representation of the aircraft dynamics. Indeed, the evaluation of stability derivatives computed around a trimmed level flight enables to determine the linear dynamics of the aircraft around that level flight. This leads to a representation of the form

$$\dot{\mathbf{q}}_{dyn} = \mathbf{A}\mathbf{q}_{dyn} + \mathbf{B}\mathbf{u}_c, \tag{22}$$

$$\mathbf{m}_{dyn} = \mathbf{C}\mathbf{q}_{dyn}, \tag{23}$$

where $\mathbf{A}$, $\mathbf{B}$, $\mathbf{C}$ are the matrices of the state space representation and $\mathbf{u}_c = [\delta_{Ail}, \delta_{VTP}, \delta_{HTP}, \delta_{th}]^T$ is the control command vector of the aircraft, including the command in angular deflection of the control surfaces and the thrust command applied to the engine. The latter is expressed as a percentage of the reference thrust $\delta_{Th,0}$, which is the command required to fly in a steady environment at the cruise speed V_∞, outside any wake. In order to further facilitate the linearization of the dynamics, we assume a complete decoupling between the lateral and the longitudinal dynamics of the aircraft. The linearized matrices and the separation in lateral and longitudinal dynamics are presented in Appendix A.

The structure of the autopilot is shown in Fig. 5; it is similar [20]. It is designed to be robust under aerodynamic interference and sufficiently simple to be integrated into existing simulation tools. It uses a full state measurement. The velocity tracking control is implemented using the three internal loops of Fig. 5 : one is proportional to the dynamic states of the aircraft ($\mathbf{K}_\mathbf{q}$), the second is proportional to the integral of the error on the side slip angle ($\mathbf{K}_\beta$), and the third one is proportional to the integral of the error on the inertial speeds ($\mathbf{K}_{V,i}$). The gains of those three first loops are designed using a linear quadratic regulator (LQR). The autopilot is designed to make the aircraft fly at 0 side slip angle i.e., $\beta^{ref} = 0°$. As an additional layer, the reference translation velocity $\boldsymbol{V}_{K,F}^{ref}$ is computed over time using three inertial position tracking loops. Each one of them implies a proportional-derivative (PD) controller that imposes the velocity target for the internal loops. Those velocities are limited through rate limiters, in order to maintain reasonable velocity targets.

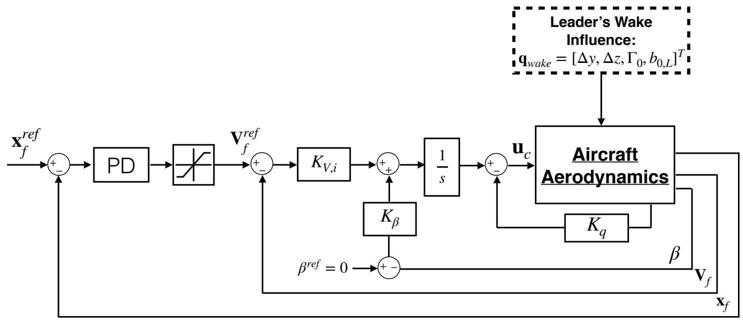

Figure 5 Complete structure of the control scheme

The autopilot, developed using linearized dynamics of the aerodynamic surrogate model, is also used as in high-fidelity simulations in order to control the dynamics of the aircraft in the reference flight environment. Indeed, as shown hereafter, there are only small differences between the natural dynamics resulting from those two representations (high-fidelity and surrogate). Consistently, the surrogate model was built in order to be sufficiently close to the high-fidelity flight simulations, but at a lower computational cost. In both cases, we can represent the controller as an additional block within the complete detection scheme (that was presented in Fig. 1), and where the aircraft aerodynamics block of Fig. 5 represents either the high-fidelity or the surrogate model. Finally, with the developed autopilot, the available measurement vector can be augmented with

$$\mathbf{m}_{\text{control}} = \mathbf{u}_c = [\delta_{Ail}, \delta_{VTP}, \delta_{HTP}, \delta_{th}]^T \ . \tag{24}$$

D. Summary of the detection strategy

The complete estimator propagates sixteen states using the surrogate model formally described by $\mathbf{f}$ and $\mathbf{h}$. Twelve states come from the dynamics of the follower $\mathbf{q}_{\text{dyn}}$ and four are the states characterizing the wake of the leader $\mathbf{q}_{\text{wake}}$. The temporal evolution of the follower's dynamic states $\boldsymbol{q}_{\text{dyn}}$ are measured by the follower to certain precision. Although the dynamics of the states of the leader's wake $\boldsymbol{q}_{\text{wake}}$ are unknown, the EnKF propagates the value of those states in order to produce an *a priori* estimate of the measurements, i.e., the vector $\mathbf{m}$. This vector is compared to the true measurement vector $\mathbf{z}$ in order to update the estimated states during the analysis step of the estimation. Thanks to classical onboard sensors (i.e., Inertial Measurements Units (IMU), Global Navigation Satellite Systems (GNSS)), the twelve dynamic states benefit from direct measurements from the follower's perspective, i.e., $\mathbf{z}_{\text{dyn}}$ are compared to $\mathbf{m}_{\text{dyn}}$. The autopilot also provides additional information thanks to the control commands and the measured aerodynamic angles, i.e., $\mathbf{z}_{\text{control}}$ (resp., $\mathbf{z}_{\text{angle}}$) are compared to $\mathbf{m}_{\text{control}}$ (resp., $\mathbf{m}_{\text{angle}}$). While the positional states $\Delta y, \Delta z$ are not directly measured by the follower, we assume the latter benefits from direct informations regarding the geometry and mass of the leader. In practice, this can be achieved using a communication tool that episodically transmits the relevant information from the leader to the follower (e.g. via an ADS-B with extended transmission capabilities). Assume that the geometrical properties of the leader are initially known, and vary little in the time scales considered. According to Eq. (10), this leads to the additional wake measurements, i.e., $\mathbf{z}_{\text{wake}}$ are compared to $\mathbf{m}_{\text{wake}}$. Taking up the notation described in Section II.B, we have

$$\begin{cases} \mathbf{q} & = \mathbf{q}_{\text{dyn}} \cup \mathbf{q}_{\text{wake}} \\ \mathbf{m} & = \mathbf{m}_{\text{dyn}} \cup \mathbf{m}_{\text{control}} \cup \mathbf{m}_{\text{angle}} \cup \mathbf{m}_{\text{wake}} \\ \mathbf{z} & = \mathbf{z}_{\text{dyn}} \cup \mathbf{z}_{\text{control}} \cup \mathbf{z}_{\text{angle}} \cup \mathbf{z}_{\text{wake}}. \end{cases} \tag{25}$$

Section IV assesses the ability of the estimator to determine the intensity of the wake of the leader in addition to determining its position. In practical terms, we will investigate the performances of the estimator when the wake measurement $\mathbf{z}_{\text{wake}} = \Gamma_{0,L}$ is not used, leading to three unmeasured wake states, namely the relative position and wake intensity i.e. $\left[\Delta y, \Delta z, \Gamma_{0,L}\right]$.

III. Cross-validation of the simulated environment and surrogate model

We validate our surrogate model by comparing the aircraft dynamic responses due to oscillating disturbances with those of an identical aircraft flying in the high-fidelity flight environment. The geometrical parameters of the generic aircraft modeled in this work are reported in Table 1. The same controller is used in both the high-fidelity flight environment and the surrogate model. To validate the latter, we analyse a scenario similar to the one presented in Fig. 2, involving a leader and a follower but without ambient turbulence. The reference parameters of the VPM simulation used to produce the high-fidelity flight environment are reported in Table 3. We used a longitudinal distance of $5b$ between the two aircraft. These conditions are not consistent with the hypothesis of extended formation flight. However, the choice of a small longitudinal separation distance was made to keep a relatively small time-to-solution for the simulation. Furthermore, the fact that the leader's vortices are not fully rolled-up when they reach the follower can be seen as a source of process noise which the estimator is designed to tolerate. Under those conditions, the simulation was run on 256 CPUs for a maximum of 5 hours.

Table 1 Geometrical parameters of the lifting surfaces of the aircraft

	Wing	**HTP**	**VTP**
Span	$b = 11m$	$b_h/b = 0.26.$	$b_v/b = 0.22$
Aspect ratio	$\text{Æ} = 7.5$	$\text{Æ}_h = 4$	$\text{Æ}_v = 4$
Shape	Ellipse	Rectangle	Rectangle
Incidence	$\alpha_{0,w} = 4°$	$\alpha_{0,h} = 1.42°$	$\alpha_{0,v} = 0°$
Sectional lift Slope	$a_0 = 2\pi$	$a_0 = 2\pi$	$a_0 = 2\pi$
Cruise speed		$V_\infty = 50m/s$	

Table 2 Parameters of the oscillating movement performed by the leader

	Config. A	**Config. B**
A_y/b	0.25	0.4
A_z/b	0.5	0.5
$\omega_y/\omega_{\text{phugoid}}$	1	0.66
$\omega_z/\omega_{\text{phugoid}}$	1	0.33

Table 3 Numerical parameters used in the VPM simulations

Domain size ($L_x \times L_y \times L_z$)	$8b \times 4b \times 2b$
Size of the cubic mesh cells	$h/b = 1/64$
Eddy Dissipation Rate (EDR)	$\epsilon^* = \frac{\epsilon b_0}{V_0{}^3} \simeq 0.02$

In this scenario, the leader aircraft is instructed to follow a sinusoidal target trajectory,

$$\boldsymbol{x}_L^{ref}(t) = \begin{bmatrix} V_\infty t \\ A_y\left[1-\cos\left(\omega_y(t-t_{\text{start}})\right)\right] \\ A_z \sin\left(\omega_z(t-t_{\text{start}})\right) \end{bmatrix}_i, \forall t > t_{\text{start}}, \text{ otherwise } \boldsymbol{x}_L^{ref}(t) = \begin{bmatrix} V_\infty t \\ 0 \\ 0 \end{bmatrix}_i, \tag{26}$$

where V_∞ is the cruise speed. The oscillations (whose parameters are reported in the *Configuration A* column of Table 2) combine changes in altitude and lateral position as we aim to assess the response of the aircraft in the (oy_iz_i) plane, which is crucial to ensure accurate wake-tracking capabilities. The frequencies are expressed in terms of the frequency of the phugoid $\omega_{\text{phugoid}} = 0.24/s$, as estimated from the linearized dynamics of Section II.C.3. Simulations (not shown here) confirm that the leader manages to perform the oscillatory maneuvers in the lateral and in the vertical directions using responsive control commands. However, a constant delay always exists both in the lateral and vertical axes between the target and the position of the aircraft mostly due to the use of speed limiters (shown in the block diagram of Fig. 6), which prevents the saturation of control commands.

The follower is instructed to maintain a prescribed position in the (oy_iz_i) plane, while evolving in close proximity of the oscillatory wake of the leader and flying at the cruise speed V_∞ along the longitudinal axis x_i. This corresponds to the *position hold* mode described in Section II.C.3. However, through aerodynamic interactions, the dynamics of the second aircraft is subjected to influence of the wake of the first one.

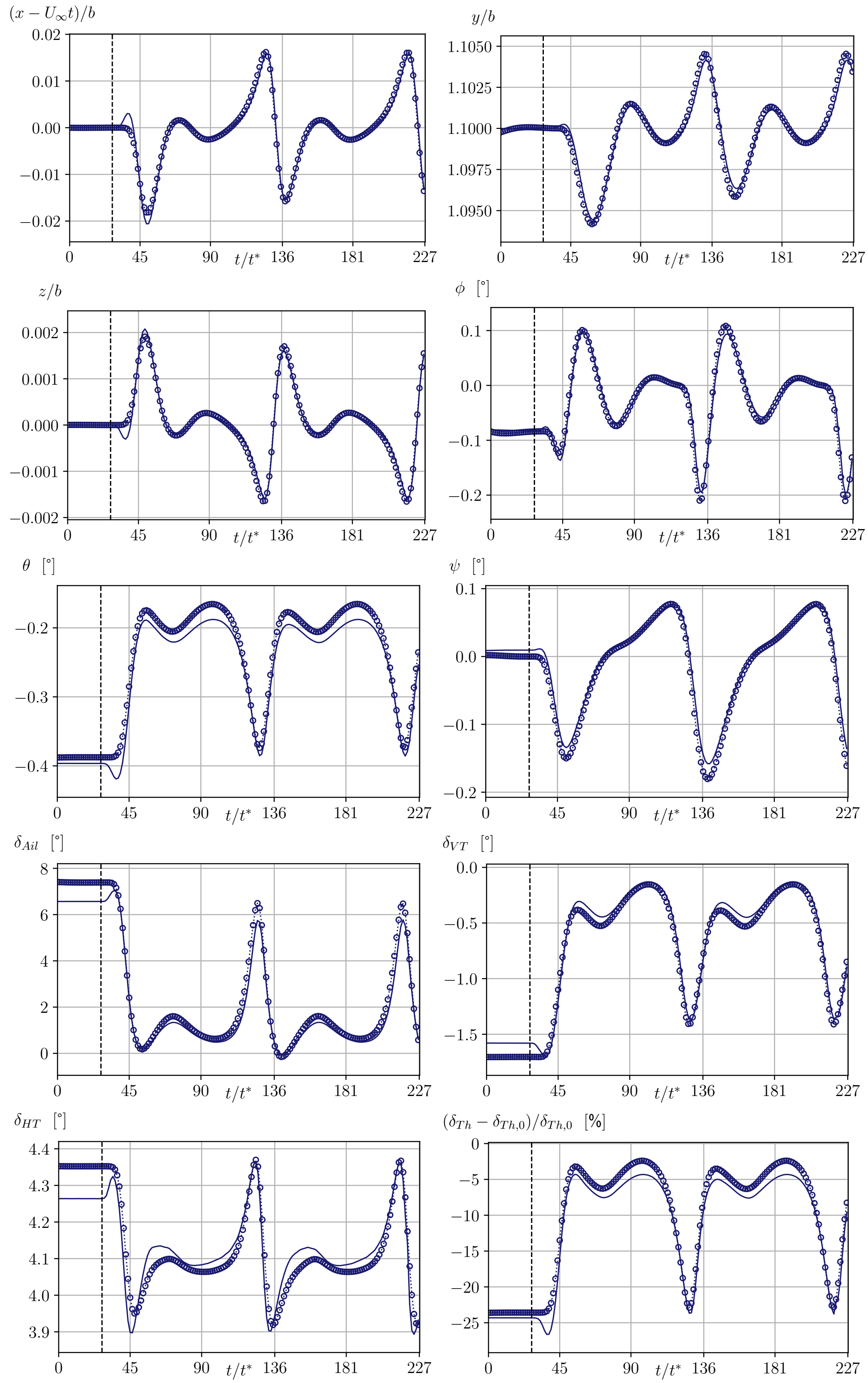

Figure 6 Dynamic response of an aircraft, maintaining its position while being impacted by an oscillating wake: comparison between the high-fidelity (—) and the surrogate dynamics (·o·). (- -) indicates the beginning of the oscillations.

Fig. 6 depicts the follower dynamics under aerodynamic loads computed by the high-fidelity flight environment and by the surrogate model. The wake starts oscillating at $t_{\text{start}} = 28t^*$, which explains the changes in the dynamic states from that time. The same autopilot and the same lifting line model were used in both the high-fidelity environment and the surrogate model, which explains their very similar behaviors. However, differences are observed either before and after t_{start} (i.e., when the wake starts oscillating), because of the hypotheses underlying the surrogate model. Indeed, as mentioned in Section II.C.1, the surrogate model assumes the wake of the leader to be made of two rolled-up counter-rotating vortex tubes. Similarly, we assume that the vortex sheet shed by the wing of the follower is fully rolled-up when it reaches the tail. Those two assumptions are not in perfect agreement with the high-fidelity flight environment, which precisely captures the rollup of the vortex sheets. This explains the offset observed on the dynamic state and, in particular, on the elevator deflection input (δ_{HT}), the pitch angle (θ), and the additional required thrust (δ_{Th}), as they are interdependent through the longitudinal dynamics. The differences in the dynamic states observed during the first moments just after the wake starts oscillating (i.e., $t \gtrapprox t_{\text{start}}$ in Fig. 6) are explained by the quasi-static hypothesis of the surrogate model; the wakes produced by the lifting lines are straight infinite vortex sheets. The impact of the moving aircraft on the sheets is instantaneous and the transient is not captured.

Despite those assumptions, the evolution of all of the 6DOF states agrees fairly well over time,illustrating the validity of the surrogate model versus the high-fidelity one. The turbulence that will be latter added to the flow will of course perturb the dynamics of the aircraft in the high-fidelity flight environment. From the estimator point of view, this corresponds to a natural source of process noise in the estimation routine.

Let us highlight several specific behaviors of the controller observed in Fig. 6. The non-zero average deflections of the ailerons and the rudder compensate for the rolling moment induced by the impacting wake and maintain 0° of slip. Also, observe that the required thrust command δ_{Th} is smaller than required by an aircraft flying outside any wake (i.e., $\delta_{Th,0}$). This reduction is to first-order approximation attributed to the rotation of the resulting aerodynamic force vector arising from the presence of the upwash induced by the leader's wake. The rotation of the force vector translates into an apparent drag reduction experienced by the follower and, therefore, to a smaller required thrust command.

An assumption of the Kalman filter is that the measurements and process disturbances are random white noise. This assumption is not exactly respected in the present case, as we have just observed biases between some of the high-fidelity measurements and the surrogate model predictions. In applications, those biases contribute to sensor errors and must be taken into account in the estimation process. A standard technique to overcome sensor biases is to augment the Kalman filter state vector with estimates of the biases. Alternative and more sophisticated techniques exist to deal with those errors and are described for instance in [44, 45]. In the present situation, the biases on all the measurements are considered negligible, they are thus not specifically tracked. They will be considered as random white noise and processed by the estimator.

IV. Results

Various simulations were performed in order to assess the efficiency of the detection and tracking strategies. We use the same parameters for the aircraft, the prescribed sinusoidal movement, and the VPM simulations as the ones used in Section III and reported in Tables 1, 2 and 3. We used the same longitudinal distance of $5b$ between the leader and the follower. Unlike the simulation described in Section III, synthetic turbulence is injected at the inlet. It is characterized by a dimensionless Eddy Dissipation Rate (EDR) $\epsilon^* = \frac{\epsilon b_0}{V_0^3} \simeq 0.02$, where $b_0 = \frac{\pi b}{4}$ and $V_0 = \frac{\Gamma_0}{2\pi b_0}$, corresponding to strong turbulence [46]. This presents a quite challenging environment to assess the performances of our estimator, as extended formation flight for energy savings is likely to be implemented under low turbulence conditions.

As described in Section II.B, the filter requires the initialization of state additive inflations $\boldsymbol{\alpha}_i$ and measurement noises $\boldsymbol{\epsilon}_i$. Additive state inflation consists of adding a sample from the Gaussian distribution $\mathcal{N}(0, \boldsymbol{\Sigma})$ to each member of the ensemble before the propagation step. The covariance matrix $\boldsymbol{\Sigma}$ is made up of a series of parameters used to tune the filter, which are provided in Appendix B. Regarding the measurements noises $\boldsymbol{\epsilon}_i$, they are directly related to the precision of the sensors used onboard the aircraft to provide the true measurements z. The measurement noise covariance matrix $\boldsymbol{V}$ is defined accordingly, i.e, as the confidence of the filter in these measurements. The covariance associated with the measurement of the side slip angle β reflects the poor quality of the measurement provided by commonly used instruments. Two different noise measurement sets are used in this work, in order to compare the influence of coarse or accurate measurements on the performance of the filter; see Section IV.A.2. They are also given in Appendix B.

This work considers two configurations of the global filtering scheme, as described in Fig. 1. Section IV.A first verifies the ability for a follower to solely use measurements coming from its dynamics in order to detect the unknown parameters of the wake produced by a leader. We also aim to quantify the accuracy of the estimated wake characteristics in this configuration, where the follower maintains a predefined trajectory $\boldsymbol{x}_f^{ref}$ using the *position hold* autopilot (switch 1 in Fig. 1). Then the follower detects the position of the wake of a leader and, at the same time, follows the appropriate position in order to constantly benefit from the largest wake upwash. In order to perform this tracking, the estimation of the position of the leader's wake $\hat{\mathbf{q}}^n_{\text{wake}}$ is provided to a wake analysis module (see Fig. 1) that filters the estimation. This provides an optimal target $\boldsymbol{x}_f^{opt}$ to be followed by the autopilot of the follower in the *wake tracking* mode (switch 2 in Fig. 1). This is described in Section IV.B.

A. Wake Detection

1. Detection of a stationary wake

This section shows that the envisioned estimation scheme is able to sense the wake and to determine the position of a non-maneuvering leader's wake over time. The leader follows a fixed target $(y_L^{ref}/b, z_L^{ref}/b) = (0, 0)$ and adapts its commands according to the perturbations in the ambient turbulence. The follower holds a position close to the optimal one in the wake of the leader $(y_F^{ref}/b, z_F^{ref}/b) = (1.1, 0)$. Both the leader and the follower fly at the cruise speed V_∞ along the x_i axis. The EnKF uses $N = 100$ ensemble members, as in the rest of this work. The estimation is performed at a rate $\Delta t_{EnKF} = 0.2 \cdot t^*$ with $t^* = \frac{b}{V_\infty}$ the convective time. The levels of noise associated with the sensor measurements are considered to be high in this section; they are provided in Appendix B.

Observe in Fig. 7 the performance of the EnKF in estimating the wake states $\mathbf{q}_{wake}$ for two filter configurations. *Filter 1* deals with a full wake measurement vector (i.e., the estimator assumes the follower knows the leader's characteristics $\mathbf{z}_{wake} = \left[\Gamma_{0,L}, b_{0,L}\right]$) whereas *Filter 2* uses only the measurement of the spacing between the vortices, i.e., $\mathbf{z}_{wake} = \left[b_{0,L}\right]$. The wake intensity $\Gamma_{0,L}$ is thus not directly provided to *Filter 2*, but along with the position of the wake (Δy and Δy) is considered to be unknown.

First consider *Filter 1*, involving the complete wake measurement vector. The convergence of the filter is obtained after 25 iterations, corresponding to a simulation time $t \simeq 5t^*$. A good estimate is obtained for the four wake states $\mathbf{q}_{\text{wake}} = \left[\Delta y, \Delta z, \Gamma_{0,L}, b_{0,L}\right]^T$. This result was expected regarding the estimation of the wake intensity $\Gamma_{0,L}$ and the spacing between the vortices $b_{0,L}$, as the estimator benefits from a direct measurement of their value through the vector $\mathbf{z}_{wake} = \left[\Gamma_{0,L}, b_{0,L}\right]$. Even though the standard deviation of the associated measurement noise was set to 30% for $\Gamma_{0,L}$ and 20% for $b_{0,L}$, the estimations remain within 5% of their actual value. Also, the confidence intervals associated to those states and computed as the *a posteriori* variance of the estimate (see Eq. (8)) remain within 15% of their actual value. However, we are more interested in the performance of the estimator in estimating the position of the wake, as no direct measurements are used by the estimator for those states. Estimates that remain within 10% of the wing span are obtained for both Δy and Δz, which is a satisfactory performance for a formation flight application. The confidence intervals for both states seem constant over the estimation process and remain within 30% of the wing span.

We now analyze the performances of *Filter 2* which uses only the spacing between the vortices as wake measurement, i.e., $\mathbf{z}_{wake} = \left[b_{0,L}\right]$, rather than $\mathbf{z}_{wake} = \left[\Gamma_{0,L}, b_{0,L}\right]$. The spacing between the vortices $b_{0,L}$ still benefits from a good estimation, because of the use of a direct measurement of that state. Like *Filter 1*, *Filter 2* converges to an accurate estimation of the vertical position Δz after 25 iterations. The main differences between the two filters appear in the estimation of $\Gamma_{0,L}$ and Δy. Indeed, *Filter 2* poorly estimates the wake intensity $\Gamma_{0,L}$; its estimate is twice the actual value with a poor confidence interval. Hemati et al.[17] had already highlighted this inaccuracy. They explained that much of the process uncertainty was lumped into the estimation of $\Gamma_{0,L}$, rather than into the position estimates Δy or Δz, which showed better accuracy in their study. However, we also observe here that the lateral position estimate Δy exhibits a significative offset, close to 30% of the wingspan. There is indeed an intrinsic correlation between $\Gamma_{0,L}$ and Δy. The inaccurate wake intensity estimation leads in fact to an over-estimated lateral-distance estimate as, from the follower's perspective, a strong distant wake generates aerodynamic effects which can hardly be distinguished from those of a closer but weaker wake. This is explained by the mechanism behind the influence of the leader's wake on the follower, which is governed by the Bio-Savart law. At first order, it is indeed proportional to the ratio $\frac{\Gamma_{0,L}}{\Delta y}$.

This observability issue was also put forward in [22] using other sets of measurements. In the present case, the

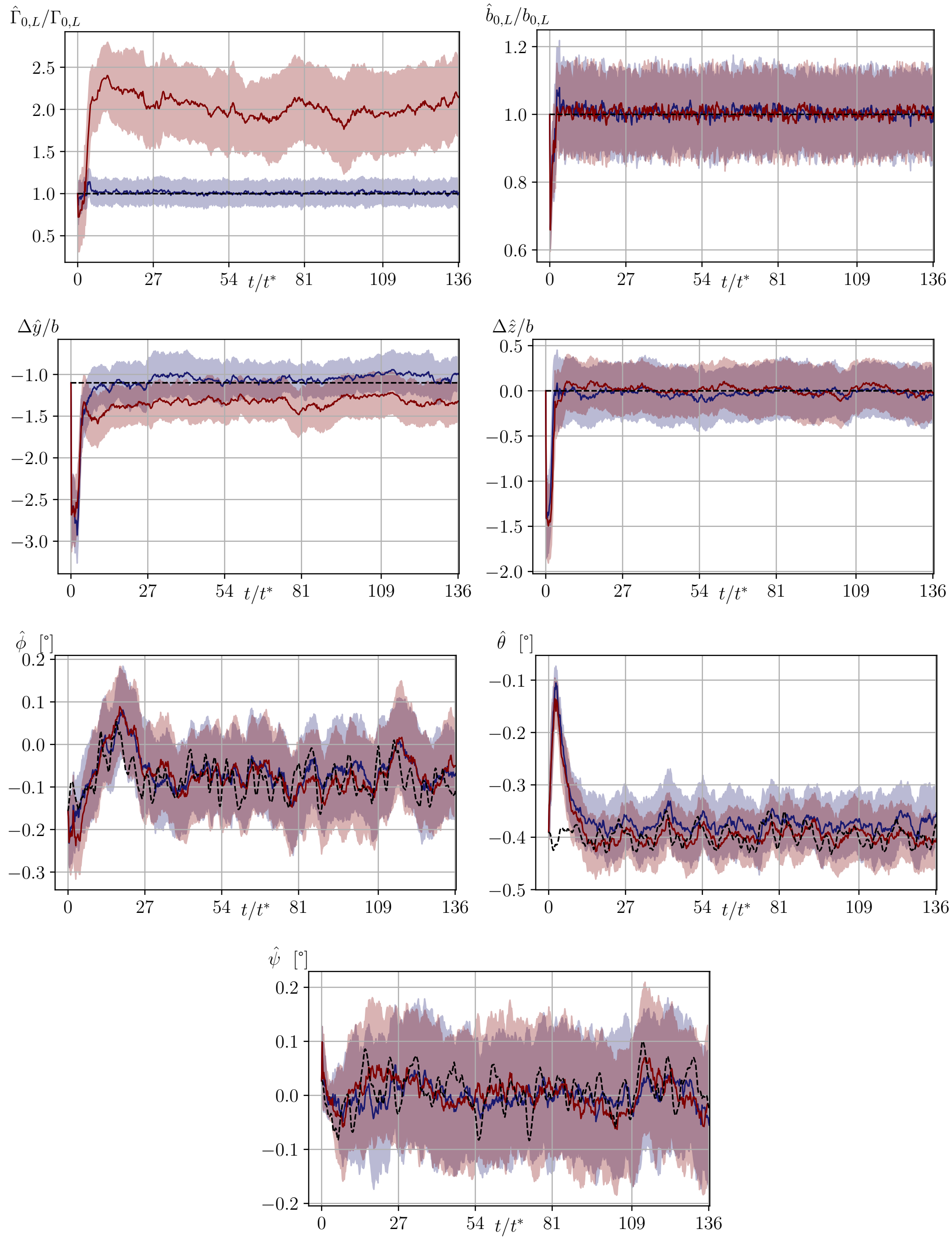

Figure 7 Detection of a steady wake. The black dotted line (⋯) indicates the actual values of the states. The blue lines (—) (resp. red (—)) are the estimates with their *a posteriori* $1-\sigma$ confidence interval produced by *Filter 1* (resp. *Filter 2*).

analysis of the dynamic states further explains this issue. For the sake of concision, we focus only on the analysis of the attitude angles of the follower, also presented in Fig. 7. Because they are also measured, the roll, pitch and yaw (as well as the position, translation velocity, and rotation rates) should be accurately estimated by the filter. The two filter configurations show similar behaviors regarding the roll and the yaw. Indeed, except for the oscillations that are attributed to the ambient turbulence, the average angles are correctly reproduced by the two filter configurations. However, the pitch angle is not estimated in the same way by the two filters, as observed in Fig. 7. *Filter 2* seems to accurately reproduce the reference pitch value on average, while the first one estimates the pitch angle with an offset that is close to the one observed in Fig. 6 where we compare the dynamics produced by the high-fidelity environment and the surrogate model. In addition to the intrinsic observability (or un-observability) correlation between $\Gamma_{0,L}$ and Δy, this initial bias is responsible for the offset observed on the wake intensity estimate $\Gamma_{0,L}$. Indeed, in not constraining $\Gamma_{0,L}$ with information provided by an ADS-B $z_{wake} = \Gamma_{0,L}$), we give the filter the opportunity to fit the dynamic states with more accuracy and, in particular, to fit the pitch angle. While adapted filter techniques exist to deal with those bias errors [44, 45], we keep our filters as simple as possible to identify the origin of the wake detection issues. Since all the states associated with the longitudinal dynamics (i.e., translations along x and z axis, and rotation about the y axis) are intrinsically correlated and, since the pitch angle measurement affects the estimation of the lateral position, we deduce that the longitudinal dynamics of the aircraft have a significant influence on the estimation of the lateral position Δy and the wake intensity $\Gamma_{0,L}$ and thus on potential errors of biases. In contrast, the vertical position Δz does not seem to be much affected by errors on the longitudinal dynamics.

It is worth mentioning that a substantial lateral estimation error has to be avoided, as it might lead to a wake encounter (i.e. the follower airplane entering one of the leader's wake vortices, leading to unwanted aircraft response and possibly severe consequences) as soon as the autopilot is switched to the *wake tracking* mode. This justifies the use of a measurement of the wake intensity $\Gamma_{0,L}$, as tested in the first configuration. Let us mention that the use of a measurement of the spacing between the wake vortices $b_{0,L}$ has a similar impact as the use of a measurement of the wake intensity $\Gamma_{0,L}$, i.e., an improved wake position estimation. We will therefore assume that $\Gamma_{0,L}$ and $b_{0,L}$ are measured in the rest of this work.

Fig. 8 presents a visual representation of the detection methodology that will be further used for a visual understanding of the processes. From the initial guess $(\Delta z/b, \Delta y/b) = (-2, -2)$, the estimated wake position converges to the exact position, then oscillates around that position. As explained in Section II.A, the high-fidelity simulations here incorporate ambient turbulence in order to accurately reproduce the environment around a flying aircraft. It explains the high frequency oscillations of the dynamics states (e.g., roll ϕ, pitch θ and yaw ψ) in Fig. 7, as well as the oscillations of the estimated position observed in Fig. 8. On the one hand, this turbulence can be seen as a model noise, as it is not reproduced in the aircraft surrogate model. On the other hand, the turbulence generates unsteadiness that might be beneficial for the detection, as it forces a movement of the follower and hence increases the observability of the process, as mentioned in [17] and [18].

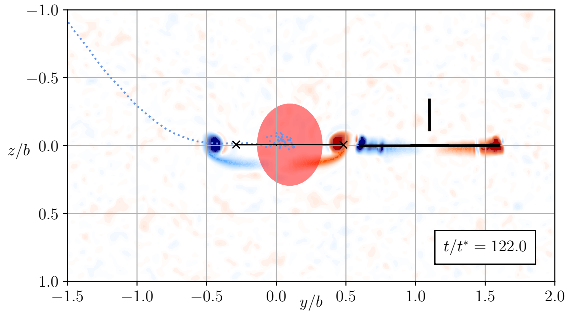

Figure 8 Cross section of the streamwise vorticity behind the follower ( ). The dotted line ( ) is the history of the estimated position of the leader's wake, with the current estimation ( ). The shaded area ( ) represents the $1-\sigma$ confidence interval of the estimate.

2. Detection of oscillating wakes

We now investigate the estimation of moving wakes, produced by a leader that follows an oscillating trajectory (identical to the one described in Section III, whose parameters are reported in the first column of Table 2). The follower is thus impacted by a wake moving up and down and from left to right; it acts so as to maintain a predefined reference position. The more unsteady the environment is, because of this strong oscillating wake, the more variations are observed in the dynamics measurements of the follower. Hypothetically, the larger the variations, the better the estimate. Indeed, large variations induced by the oscillating leader tend to overcome the measurement error or the model error. This means that more accurate estimations should be obtained when the follower is close to the wake. From the follower's perspective, the observability of the process might thus improve, when subjected to an unsteady wake. We investigate this assumption in the following example.

In this study case, the follower holds the same position as previously, $(y_F^{ref}/b, z_F^{ref}/b) = (1.1, 0)$, at a distance of $5b$ behind the leader. Periodic patterns similar to those of Fig. 6 are then observed on the follower's dynamics, reflecting the unsteady aerodynamic forces induced by the oscillating leader's wake. The EnKF estimations of the aerodynamic states $\mathbf{q}_{\text{wake}}$ and the attitude of the follower are displayed in Fig. 9. Two different filter configurations are also compared in this figure. While in Section IV.A.1, we evaluated the impact of the use of the measurement $z = \Gamma_{0,L}$, we here highlight the impact of the measurement noise $\boldsymbol{\epsilon}_i$ on the detection performances.

The first configuration in Fig. 9 uses the exact same parameters that are used in the *Filter 1* configuration of Fig. 7. In particular, the measurement noise levels $\boldsymbol{\epsilon}_i$ are assumed to be high on every measurement. In other terms, it means the filter does not have much confidence in the true measurements $\boldsymbol{z}$ that it receives from the flight environment. We observe that in such a situation, the aircraft is not able to discern the oscillatory movement of the wake of the leader. At the beginning of the detection procedure, the filter locks on to the initial steady position of the wake. The wake

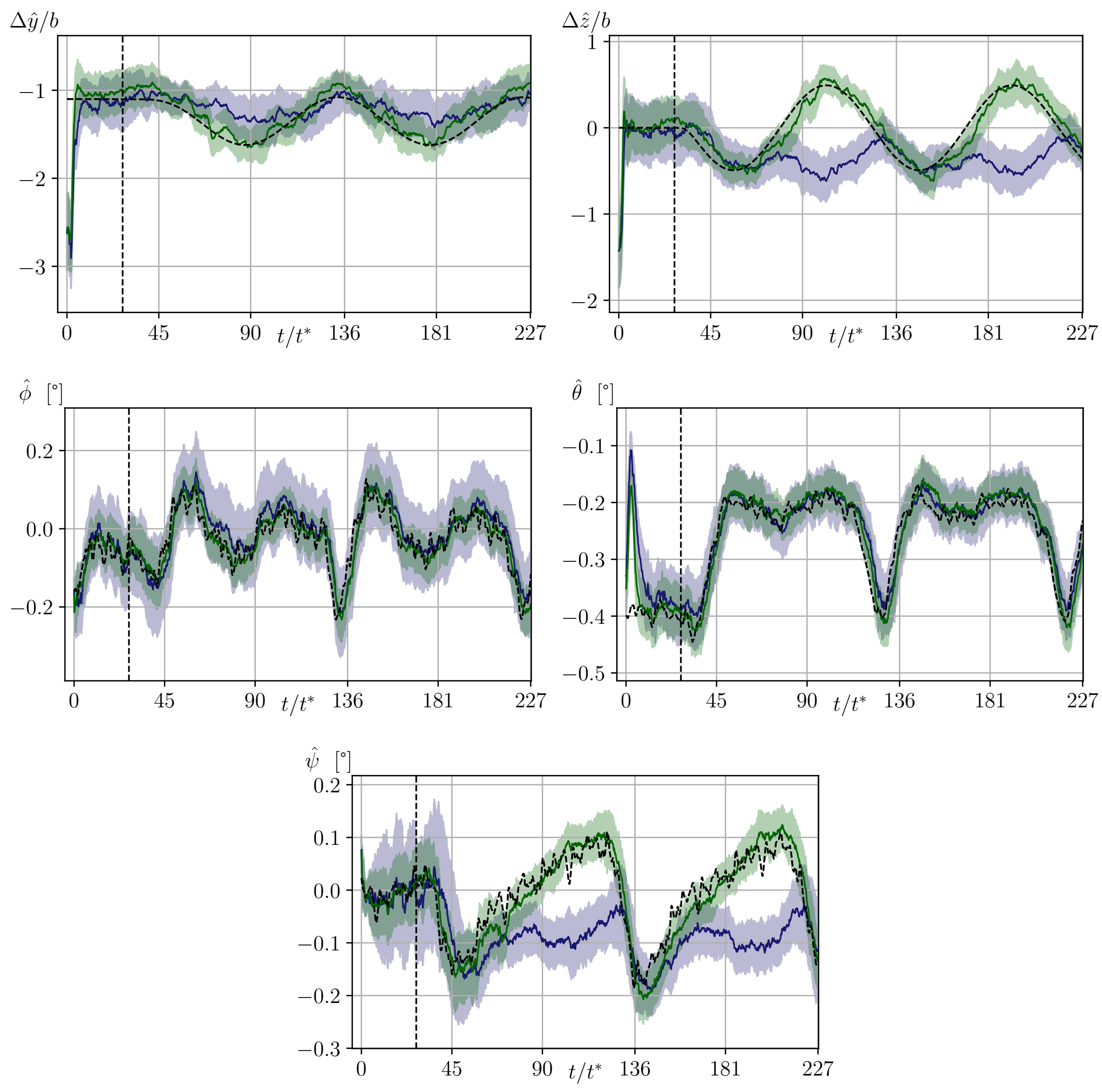

Figure 9 Detection of an oscillating wake. The black dotted line (⋯) indicates the actual values of the states. The blue lines (—) (resp. green (—)) are the estimates with their *a posteriori* $1-\sigma$ confidence interval produced by *Filter 1* (resp. *Filter 3*).

then starts to oscillate moving up and translating to the left, compared to the position of the follower. While the filter identifies the upward movement, it is not further able to sense the downward movement. This is because the wake also moves away to the left, which leads to a reduction of the aerodynamic influence of the wake on the aircraft. In practice, because the noise levels $\boldsymbol{\epsilon}_i$ are high, the filter does not accurately estimate the dynamic states of the follower, which further translates into errors in estimating the wake position. Indeed, observe in Fig. 9 that, contrary to the roll and pitch angles, the yaw angle is not properly estimated. The need of a better estimation of the yaw angle is explained by the fact that the autopilot of the follower is designed to make it fly at 0° side slip angle, even under the influence of an external wake. When the leader's wake is moving, it modifies the flow field around the follower and therefore the angle of slip perceived by the follower. The autopilot reacts to this modification, which translates into a change in the yaw angle. An inaccurate estimation of the yaw angle leads therefore to incorrect wake position estimates. This observation suggests that the lateral dynamics of the follower have a strong influence in the detection of the vertical relative position Δz.

We therefore consider a third filter configuration (*Filter 3*), in which we assume lower noise levels regarding the three attitude angles. Rather than the noise levels $V_\phi = V_\theta = V_\psi = 1°$ of *Filter 1*, we decrease them tenfold, i.e., $V_\phi = V_\theta = V_\psi = 0.1°$ for *Filter 3*. Observe in Fig. 9 that this second filter estimates the yaw angle more accurately, which leads to a proper estimation of the position of the wake even when its position relative to the follower increases. Also observe that the standard deviation of the relative position estimates are smaller when using lower noise levels, because of improved confidence in the attitude measurements. In this simulation, the relative distance between the center of the wake and the follower barely exceeds $1.5b$. Accurate sensors and confidence in the measurements are required to obtain acceptable estimations. This will be even more the case at larger distances since the farther apart the wake and the follower are, the weaker the aerodynamic interferences become. Therefore, even if the relative motion between the wake and the follower helps in the detection, too large a relative distance will degrade the sensitivity. These behaviors will depend on the accuracy of the measurements processed by the estimator as well as the ability of the surrogate model to represent the high-fidelity flight environment.

Fig. 10 shows the estimated position of the vortices during the estimation process assuming low noise levels (i.e., using *Filter 3*), superimposed to the actual vorticity field. Even if the instantaneous estimation is not accurate, it is always located in the vicinity of the actual wake vortices and it reproduces the trajectory of the wake of the leader on average. The estimator thus shows robustness in the estimation process and is therefore a suitable tool to maintain an optimal position in the wake of a leader.

B. Wake Tracking

Let us now investigate the ability of the follower to maintain in real time a constant position relative to a leader's wake. Taking advantage of the estimation of the position of the wake over time, the follower actively targets the optimal location in order to benefit from maximum fuel burn reduction at all times. In the investigated scenario, the leader also performs a sinusoidal oscillating trajectory. The period of oscillation was selected in order to be larger than the time response of the autopilot (see the second column of Table 2). Indeed, in particular for the lateral behavior, the tracking of the leader's wake by too slow an autopilot may lead to a wake encounter, which is a situation that a conventional autopilot is not able to deal with. In this section, we use *Filter 3* described in Section IV.A.2, i.e., we consider an EnKF that uses the complete wake measurement vector ($z_{wake} = \left[\Gamma_{0,L}, b_{0,L}\right]$) and assume lower noise levels regarding the three attitude angle measurements. The estimate of the position of the leader's wake $\hat{\mathbf{q}}^n_{\text{wake}}$ is provided to a wake analysis module (see Fig. 1) that filters it and provides an optimal target $\boldsymbol{x}_F^{opt}$ to be followed by the autopilot of the follower in the *wake tracking* mode (switch 2 in Fig. 1). A Double Exponential Moving Average (DEMA) is used to filter the

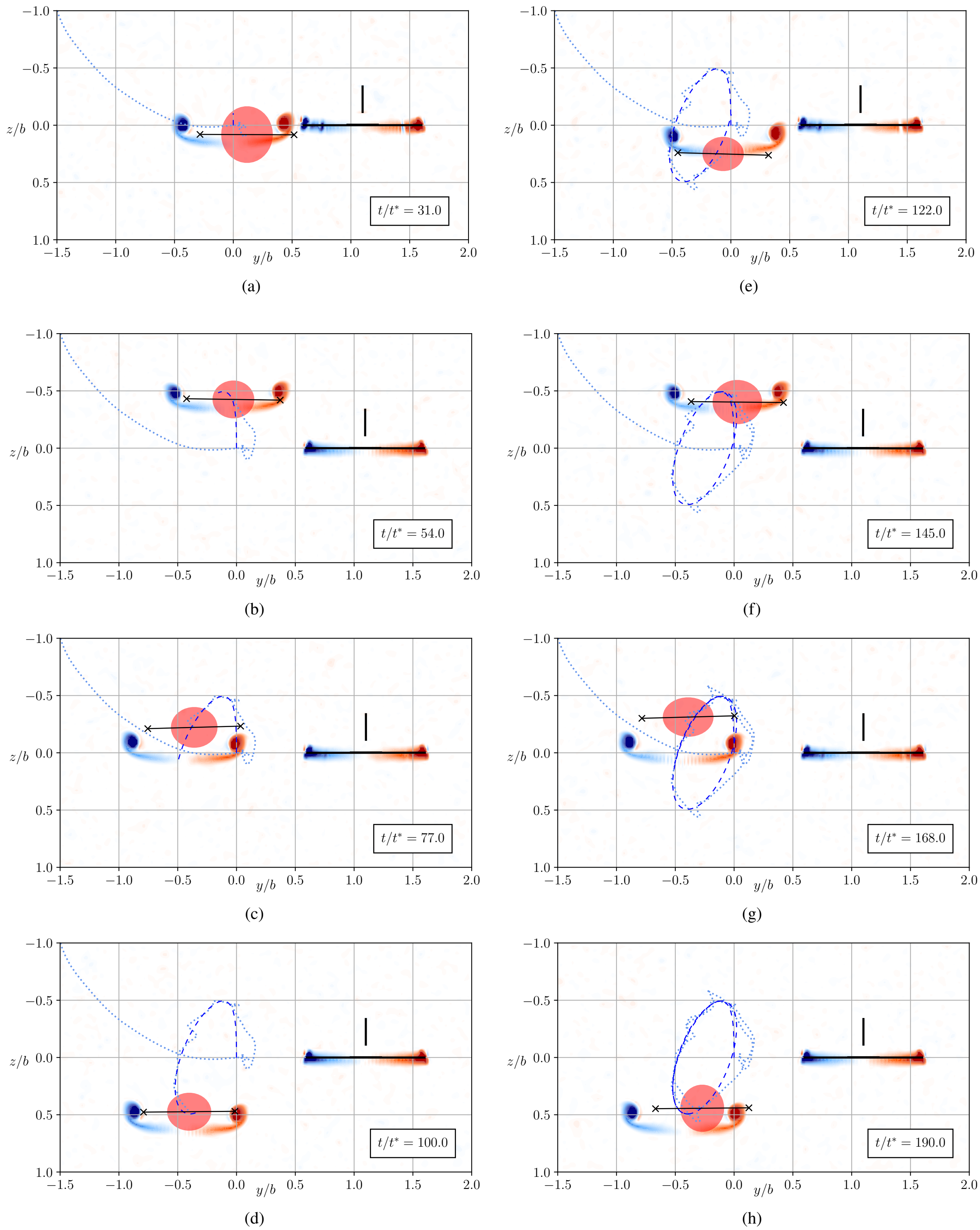

Figure 10 Vortex system estimated by the EnKF over time. The background shows the vorticity behind the follower. The blue dotted line (⋯) is the history of the estimated position with its $1-\sigma$ confidence interval ( ). The blue dashed line (- -) is the actual trajectory of the leader's wake.

relative position estimates Δy and Δz in order to provide a smooth target to the autopilot of the follower.

The target has an offset $(\Delta y^{ref}/b, \Delta z^{ref}/b) = (-1.1, 0)$ from the wake estimated position which is close to the optimal position. Along the stream-wise direction, the autopilot of the aircraft is instructed to maintain a constant speed V_∞. The performance of the complete tracking strategy involving the EnKF and the filtered target provided to the follower is represented in Fig. 11.

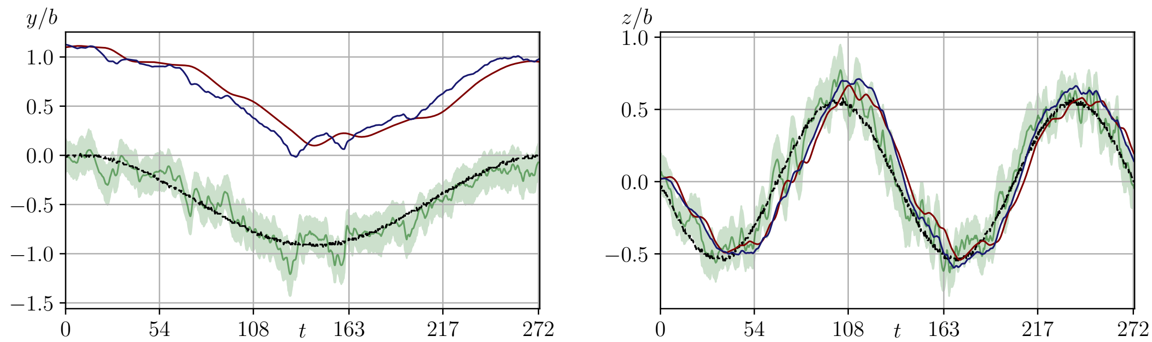

Figure 11 Performance of the EnKF in *wake tracking* mode. The green solid lines (—) (resp. black dashed (····)) are the estimates (resp. actual values) of the wake's position. The blue solid line (—) is the target provided to the follower and the red solid line (—) is the actual trajectory of the follower.

The estimator shows similar performances as the one observed for the second filter in Section IV.A.2. The reference lateral and vertical positions are indeed accurately detected by the estimator, due to the use of a direct measurement of the wake intensity (as discussed in Section IV.A.1) and low noise levels (as discussed in Section IV.A.2). When comparing the actual trajectory of the follower and the target provided to its autopilot, we observe that the follower accurately tracks this offset target. A time delay still remains between the trajectory of the follower and the position of the wake over time, which is explained by the delay induced by an autopilot that is not fast enough to track a target without delay, as already mentioned in Section III. The target itself also presents a small delay as it results from a smoothing of the estimated position of the wake. This estimation is indeed delayed compared to the exact position of the wake because of the time response of the estimator.

Fig. 12 presents a visual interpretation of the tracking strategy, and shows instantaneous views of the flow in the cross section $x = x_F$. Even if the instantaneous estimated position of the wake is noisy and does not perfectly fit with the exact position of the wake, it is always located in the vicinity of the actual wake. Indeed, the estimation errors remain within 20% of the wing span. On average, the follower reproduces the same oscillating pattern as the one produced by the leader's wake.

By maintaining a nearly constant position relative to the wake, the follower always remains close to the leader's wake. It therefore benefits from a stronger influence, which leads to an improved estimation as already observed in Section IV.A.2. The use of the control commands as measurements becomes even more important in the detection, as it gives a direct information of the loads perceived by the follower while it is moving.

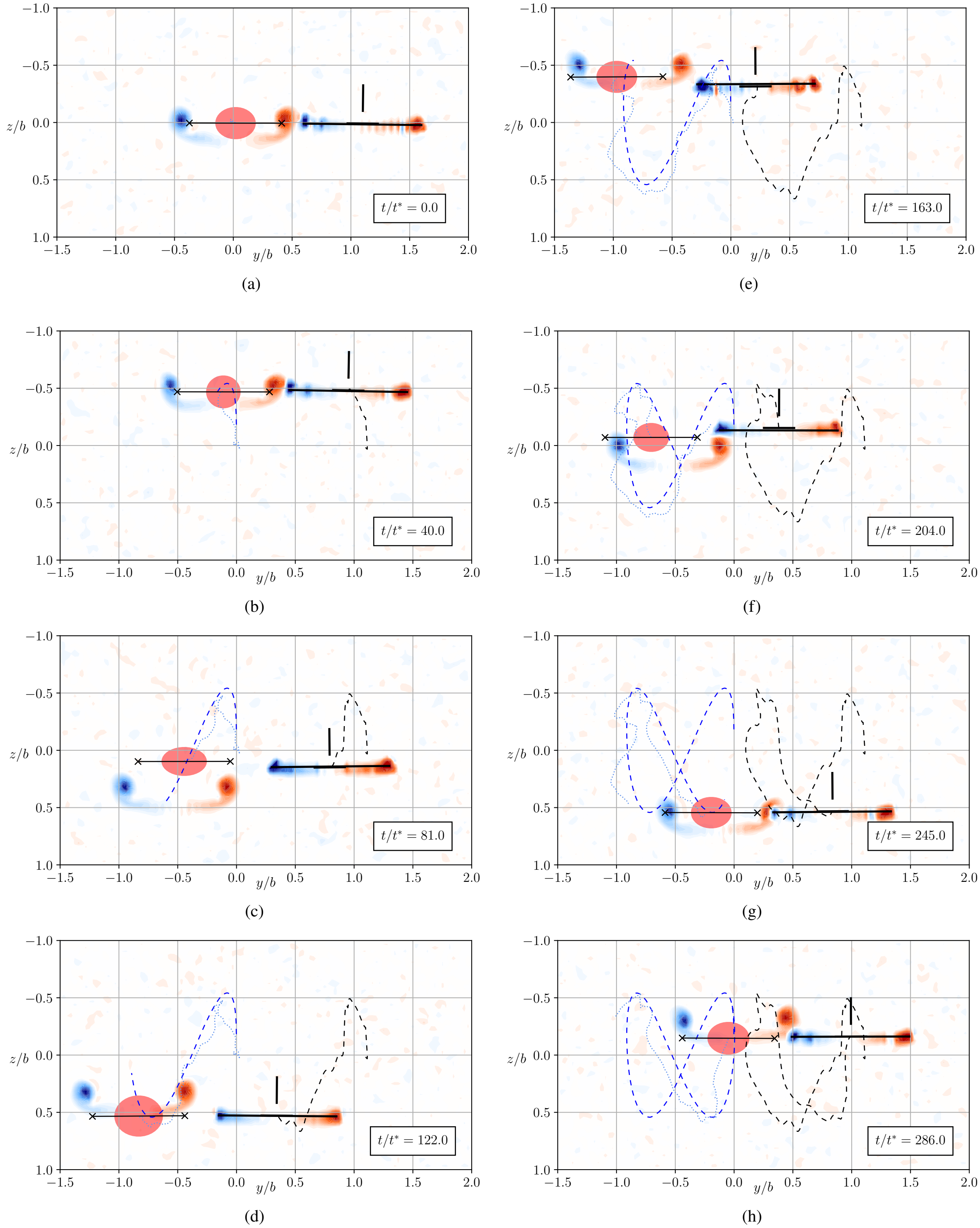

Figure 12 Vortex system estimated by the EnKF over time. The background shows the vorticity behind the follower. The blue dotted line (⋯) is the history of the estimated position with its $1-\sigma$ confidence interval ( ). The blue dashed line (- -) (resp. black (- -)) is the history of the exact position of the wake (resp. of the follower).

As already observed in Section III, by staying in the close vicinity of the wake of the leader, the follower benefits from a decrease of the thrust required to follow a trajectory, because of an apparent drag reduction. We study the variation of the thrust command δ_{Th} applied during the *wake tracking* strategy compared to the reference thrust $\delta_{Th,0}$ of an isolated, steady aircraft. This *wake tracking* follower applies a time-varying thrust command $\delta_{Th}(t)$ as it adapts to the oscillating wake produced by the leader, that periodically oscillates at the frequency ω (given in Table 2). The thrust command therefore shows large oscillations: the increase in amplitude is due to the change in altitude of the follower that maintains a constant relative position with the leader. High thrust corresponds to climb phases and low thrust to the descending parts of the wake oscillations. To evaluate the real impact of the wake on the thrust required by a *wake tracking* follower, we compute the average thrust command over time:

$$\overline{\delta}_{Th} = \frac{1}{T}\int_{t}^{t+T} \delta_{Th}(t)dt, \tag{27}$$

where $T = \frac{2\pi}{\omega}$ is the leader's wake oscillating period, see Table 2. This gives an average thrust reduction $(\overline{\delta}_{Th} - \delta_{Th,0})/\delta_{Th,0} = -22\%$ compared to an aircraft flying outside any formation (i.e. $\delta_{Th,0}$). This reduction is to be compared to the -24% thrust reduction performed by a similar aircraft maintaining the optimal position (i.e. $(y_F^{ref}/b, z_F^{ref}/b) = (1.1, 0)$) in the wake of a fixed leader ($(y_L^{ref}/b, z_L^{ref}/b) = (0, 0)$), as described in Section IV.A.1 i.e. the *position hold* configuration. The lower thrust reduction observed during the *wake tracking* configuration is explained by the lag between the actual position of the wake and the position of the follower, as highlighted in Fig. 11. The follower is never positioned at the exact optimal position at the exact optimal time, as it tracks a moving position that it has to estimate first. However, we also compare the -22% thrust reduction of the *wake tracking* strategy to the -6% reduction performed by a similar aircraft maintaining a fixed position behind a moving leader, as described in Section IV.A.2. We conclude that even if we do not meet the maximal drag reduction possible, the *wake tracking* strategy enables to increase the performance of formation flight compared to a passive positioning.

However, the energy savings predicted here above have to be considered prudently and with nuance. They are indeed larger than those measured during experimental studies [4, 5]. The present setup will in fact lead to an over-prediction as it neglects any fuselage drag, uses idealized airfoil polars, and the aircraft are not flying at the maximum range operating point, i.e., $C_{d,\text{parasitic}} < C_{d,\text{induced}}$. Despite those differences, this setup proves that the active *wake tracking* strategy enables a significant improvement in drag reduction and hence increases the benefits in flying in formation.

V. Conclusions

This work proposes a potential wake detection strategy based on aircraft flight dynamics measurements that a follower might adopt when flying in the vicinity of the wake of a leader in extended formation flight for energy savings. It extends the approach of Caprace et al. [22] based on an Ensemble Kalman Filter for the estimation of the position of the leader's wake relative to the position of the follower.

Large Eddy Simulations of the wake generated by two-aircraft formations in ambient turbulence produce a high-fidelity flight environment. Aerodynamic loads are computed on each lifting surfaces of the aircraft. One can then integrate the 6 degrees-of-freedom (6DOF) dynamics of each aircraft over time and control their trajectories through the use of a simple autopilot. The EnKF uses measurements of the follower's dynamics and estimates the relative position of the leader's wake in comparing them to a simplified yet accurate surrogate model of the two-aircraft formation dynamics.

Two flight configurations were investigated in this work. First, the follower is tasked with a *position hold*; this configuration is used to assess the performances of the estimator. The sole follower dynamics measurements were found to be sufficient to detect the relative vertical and lateral positions of the wake of the leader, as long as the follower is provided informations regarding the mass and geometry of the leader.

The second configuration involved a *wake tracking* strategy. The estimator performed similar to that of the first configuration in terms of detection accuracy, while at the same time the follower was performing the desired tracking maneuvers in a turbulent environment. The current study has also proven the efficiency of a tracking strategy in terms of thrust reduction. To the authors' knowledge, this constitutes the first time a wake-tracking controller is shown to be effective in determining in real time the relative distance between the wake of a leader and the follower itself, in order to maintain a chosen relative position, without the need for dedicated hardware equipment.

For both configurations, the use of dynamics measurements augmented by an indirect measure of the leader's wake intensity proves sufficient to detect the position of a leader's wake when fed to the EnKF. Such a scenario was motivated by its relatively short-term feasibility: on current aircraft, an Inertial Measurements Unit, a Global Navigation Satellite System and an Automatic Dependent Surveillance-Broadcast receiver are readily available. Also, the need for an indirect measure of the leader's wake intensity is explained by the mechanism behind the influence of the wake on the follower which is governed by the Bio-Savart law. Indeed, the latter implies an intrinsic correlation between the wake intensity and the relative position of the wake which leads to observability issues when using aircraft dynamics as unique measurements.

Therefore, the sole requirement is the design of an estimator surrogate model that represents accurately enough the aircraft dynamics and the influence of the wake of the leader. The effects of this accuracy on detection performance have been assessed. First, biases between the *actual* measurements (here provided by the high-fidelity flight environment) and the simulated measurements provided by the surrogate model can lead to significant biases in the estimation of the position of the leader's wake. These errors seem to be amplified by the observability issues discussed above. On a related note, the lateral dynamics have been shown to govern the detection of the vertical relative position of the leader's wake, while the longitudinal dynamics, the lateral relative position. It is finally observed that the estimator struggles to detect the position of the wake, if the measurement noise levels are high. The estimator has showed improved performances when lower measurement noise levels were considered regarding the attitude angle measurements. In practice, this consists of assuming the use of accurate sensors aboard the aircraft.

Appendix

A. Open-loop dynamics of the aircraft and autopilot parameters

The longitudinal dynamics is given through the following states, measurements and matrices:

$$\mathbf{q}_{long} = \begin{pmatrix} u_{K,F} & w_{K,F} & q & \theta & x_F & z_F \end{pmatrix}^T, \quad \mathbf{u}_{long} = \begin{pmatrix} \delta_{HT} & \delta_{Th} \end{pmatrix}^T$$

$$\mathbf{m}_{long} = \begin{pmatrix} u_{K,F} & w_{K,F} & q & \theta & x_F & z_F & \alpha & \gamma & U_{K,F} & W_{K,F} \end{pmatrix}^T$$

$$\mathbf{A_{long}} = \begin{pmatrix} -0.005238 & 0.1233 & 0 & 10 & 0 & 0 \\ -0.4071 & -3.1058 & 48.23 & 0 & 0 & 0 \\ 0.006310 & -0.3968 & -4.111 & 0 & 0 & 0 \\ 0 & 0 & 1 & 0 & 0 & 0 \\ 1 & 0 & 0 & 0 & 0 & 0 \\ 0 & 1 & 0 & -50 & 0 & 0 \end{pmatrix}, \quad \mathbf{C_{long}} = \begin{pmatrix} 1 & 0 & 0 & 0 & 0 & 0 \\ 0 & 1 & 0 & 0 & 0 & 0 \\ 0 & 0 & 1 & 0 & 0 & 0 \\ 0 & 0 & 0 & 1 & 0 & 0 \\ 0 & 0 & 0 & 0 & 1 & 0 \\ 0 & 0 & 0 & 0 & 0 & 1 \\ 0 & 0.02 & 0 & 0 & 0 & 0 \\ 0 & -0.02 & 0 & 1 & 0 & 0 \\ 1 & 0 & 0 & 0 & 0 & 0 \\ 0 & 1 & 0 & -50.00 & 0 & 0 \end{pmatrix}$$

$$\mathbf{B_{long}} = \begin{pmatrix} -0.04022 & -1.468 & -3.426 & 0 & 0 & 0 \\ 0.001429 & 0 & 0 & 0 & 0 & 0 \end{pmatrix}^T$$

The lateral dynamics is given through the following states, measurements and matrices:

$$\mathbf{q}_{lat} = \begin{pmatrix} v_{K,F} & p & r & \phi & \psi & y_F \end{pmatrix}^T, \quad \mathbf{u}_{lat} = \begin{pmatrix} \delta_{Ail} & \delta_{VT} \end{pmatrix}^T, \quad \mathbf{m}_{lat} = \begin{pmatrix} v_{K,F} & p & r & \phi & \psi & y_f & \beta & V_{K,F} \end{pmatrix}^T$$

$$\mathbf{A_{lat}} = \begin{pmatrix} -0.2150 & -0.5311 & -48.70 & 10 & 0 & 0 \\ -0.2844 & -11.42 & 3.315 & 0 & 0 & 0 \\ 0.3396 & 0.6015 & -2.050 & 0 & 0 & 0 \\ 0 & 1 & 0 & 0 & 0 & 0 \\ 0 & 0 & 1 & 0 & 0 & 0 \\ 1 & 0 & 0 & 0 & 0 & 0 \end{pmatrix}, \qquad \mathbf{C_{lat}} = \begin{pmatrix} 1 & 0 & 0 & 0 & 0 & 0 \\ 0 & 1 & 0 & 0 & 0 & 0 \\ 0 & 0 & 1 & 0 & 0 & 0 \\ 0 & 0 & 0 & 1 & 0 & 0 \\ 0 & 0 & 0 & 0 & 1 & 0 \\ 0 & 0 & 0 & 0 & 0 & 1 \\ 0.02 & 0 & 0 & 0 & 0 & 0 \\ 1 & 0 & 0 & 0 & 50 & 0 \end{pmatrix}$$

$$\mathbf{B_{lat}} = \begin{pmatrix} 0 & -3.910 & 0.06832 & 0 & 0 & 0 \\ -1.075 & -1.422 & 1.698 & 0 & 0 & 0 \end{pmatrix}^T$$

The state-space velocity-tracking part of the autopilot is made up of the state-proportional gain matrices:

$$\mathbf{K_{q_{long}}} = \begin{pmatrix} -0.04317 & 0.5569 & -2.305 & -49.03 & 0 & 0 \\ 3728 & 29.26 & 439 & 7291 & 0 & 0 \end{pmatrix}$$

$$\mathbf{K_{q_{lat}}} = \begin{pmatrix} -2.963 & -1.845 & -3.371 & -25.85 & -153.2 & 0 \\ -0.7370 & 0.07704 & 4.583 & -2.825 & -6.093 & 0 \end{pmatrix}$$

and of the integrative part whose gain matrices are given by

$$\mathbf{K_{V_{x,i}}} = \begin{pmatrix} 0.03760 \\ 9998 \end{pmatrix}, \quad \mathbf{K_{V_{y,i}}} = \begin{pmatrix} -1.742 \\ -0.09760 \end{pmatrix}, \quad \mathbf{K_{V_{z,i}}} = \begin{pmatrix} 1.7450 \\ -215.4 \end{pmatrix}, \quad \mathbf{K}_{\beta} = \begin{pmatrix} 5.592 \\ -99.83 \end{pmatrix}$$

As explained in Section II.C.3, the feedback gains are designed using a Linear Quadratic Regulator (LQR), much akin to what is done in [20]. We initialize the parameters of the LQR controller so that the resulting gains allow a high-speed tracking and responsive control commands. Under these conditions, the obtained gains are therefore important compared to the ones observed in classical control loops.

The inertial position-tracking part of the autopilot is made up of the P-D compensators,

$$k_{Px_i} = 0.8, \qquad k_{Py_i} = 0.35, \qquad k_{Pz_i} = 0.75$$

$$k_{Dx_i} = 0.1, \qquad k_{Dy_i} = -0.00025, \qquad k_{Dz_i} = 0$$

and of the rate limiters

$$\frac{|U_i|_{max}}{V_\infty} = 0.1, \qquad \frac{|V_i|_{max}}{V_\infty} = 0.02, \qquad \frac{|W_i|_{max}}{V_\infty} = 0.06$$

B. EnKF parameters

The measurement noise $\boldsymbol{\epsilon}_i$ and the state inflation $\boldsymbol{\alpha}_i$ are random variables that follow zero-mean normal distributions,

$$\begin{cases} \boldsymbol{\epsilon}_i \sim \mathcal{N}(0, \mathbf{V}_{\text{err}}) \\ \boldsymbol{\alpha}_i \sim \mathcal{N}(0, \boldsymbol{\Sigma}). \end{cases} \tag{28}$$

The covariance matrices $\mathbf{V}$ and $\boldsymbol{\Sigma}$ are diagonal and constant over the estimation process. The inflation variance associated to each one of the states are fine tuned from the analysis of the dynamics of an aircraft (see Fig. 6). Adjustments were performed as we went along a larger number of simulations, and on a case-by-case basis for each one of the states or measurements. The values used in the simulations are given in Table 4.

The noise level variances associated to each one of the measurements are related to the precision of the sensors used in a real application, and to the accuracy of the surrogate model used in the filter. We define two sets of measurement variances. The first one refers to the "high noise levels" (i.e. *Filter 1* and *Filter 2*). The second one refers to "low noise levels" (i.e. *Filter 3*) and differs from the first one with a reduction of the noise levels associated to attitude angles only. The values used in the simulations are given in Table 5

Funding Sources

This project has received funding from the European Research Council (ERC) under the European Union's Horizon 2020 research and innovation program (grant agreement No. 725627).

The development work benefited from the computational resources provided by the supercomputing facilities of the Université catholique de Louvain (CISM/UCL) and the Consortium des Équipements de Calcul Intensif (CÉCI) en Fédération Wallonie Bruxelles (FWB) funded by the Fond de la Recherche Scientifique de Belgique (F.R.S.-FNRS) under Convention No. 2.5020.11. The present research also benefited from computational resources made available on the Tier-1 supercomputer of the Fédération Wallonie-Bruxelles, infrastructure funded by the Walloon Region under the grant agreement No. 1117545.

Table 4 Additive inflation variance associated to each one of the states (i.e. diagonal of the matrix Σ)

x_F/b	0.00003	ϕ	0.0004°
y_F/b	0.0005	θ	0.0003°
z_F/b	0.0003	ψ	0.0004°
U_F/V_∞	0.000006	pb/V_∞	0.0001°
V_F/V_∞	0.00006	qb/V_∞	0.00006°
W_F/V_∞	0.00006	rb/V_∞	0.00008°
$\Delta y/b$	0.04	$\Gamma_{0,L}/\overline{\Gamma}_{0,L}$	0.05
$\Delta z/b$	0.04	$b_{0,L}/b$	0.05

Table 5 Noise level variances associated to each measurement (i.e. diagonal of the matrix V) for the two sets envisioned in this study

	High levels	Low levels
x_F/b	0.1	0.1
y_F/b	0.1	0.1
z_F/b	0.1	0.1
U_F/V_∞	0.002	0.002
V_F/V_∞	0.002	0.002
W_F/V_∞	0.002	0.002
ϕ	1°	0.1°
θ	1°	0.1°
ψ	1°	0.1°
pb/V_∞	0.02°	0.02°
qb/V_∞	0.02°	0.02°
rb/V_∞	0.02°	0.02°
δ_{Ail}	1°	1°
δ_{VT}	1°	1°
δ_{HT}	1°	1°
$\delta_{Th}/\delta_{Th,0}$	0.1	0.1
α	1°	1°
β	1°	1°
$\Gamma_{0,L}/\overline{\Gamma}_{0,L}$	0.3	0.3
$b_{0,L}/\overline{b}_{0,L}$	0.2	0.2

References

[1] Wieselsberger, C., “Beitrag zur Erklärung desWinkelfluges einiger Zugvogel,” *Zeitschrift fur Flugtechnik und Motorluftschiffahrt*, Vol. V, No. 15, 1914, pp. 225–229.

[2] Schlichting, H., “Leistungsersparnis im Ver-bandsflug,” *Mitt. Dt. Akad. Luftforschung*, Vol. H, No. 2, 1942, pp. 97–135.

[3] Hummel, D., “The Use of Aircraft Wakes to Achieve Power Reductions in Formation Flight,” *The Characterization & Modification of Wakes from Lifting Vehicles in Fluid*, Vol. AGARD-CP-584, NATO, 1996, pp. 1–13.

[4] Beukenberg, M., and Hummel, D., “Aerodynamics, Performance and Control of Airplanes in Formation Flight,” *ICAS, Congress, 17 th, Stockholm, Sweden, Proceedings.*, 1990, pp. 1777–1794.

[5] Vachon, M., Ray, R., Walsh, K., and Ennix, K., “F/A-18 Aircraft Performance Benefits Measured during the Autonomous Formation Flight Project,” Tech. Rep. TM-2003-210734, NASA, 2002. doi:10.2514/6.2002-4491.

[6] Hanson, C. E., Pahle, J., Reynolds, J. R., and Andrade, S., “Experimental Measurements of Fuel Savings During Aircraft Wake Surfing,” *2018 Atmospheric Flight Mechanics Conference*, 2018, p. 3560. doi:10.2514/6.2018-3560.

[7] Flanzer, T. C., Bieniawski, S. R., and Brown, J. A., "Advances in Cooperative Trajectories for Commercial Applications," *AIAA Scitech 2020 Forum*, 2020. doi:10.2514/6.2020-1257, URL https://arc.aiaa.org/doi/abs/10.2514/6.2020-1257.

[8] Ning, A., Flanzer, T. C., and Kroo, I. M., "Aerodynamic Performance of Extended Formation Flight," *Journal of Aircraft*, Vol. 48, No. 3, 2011, pp. 855–865. doi:10.2514/1.C031046.

[9] Bieniawski, S. R., Rosenzweig, S., and Blake, W. B., "Summary of Flight Testing and Results for the Formation Flight for Aerodynamic Benefit Program," *52nd Aerospace Sciences Meeting*, AIAA, 2014, pp. 1–26. doi:10.2514/6.2014-1457.

[10] Edstrand, A. M., Davis, T. B., Schmid, P. J., Taira, K., and Cattafesta, L. N., "On the Mechanism of Trailing Vortex Wandering," *Journal of Fluid Mechanics*, Vol. 801, 2016. doi:10.1017/jfm.2016.440.

[11] Unterstrasser, S., and Stephan, A., "Far Field Wake Vortex Evolution of Two Aircraft Formation Flight and Implications on Young Contrails," *The Aeronautical Journal*, Vol. 124, No. 1275, 2020, pp. 667–702. doi:10.1017/aer.2020.3.

[12] Holzäpfel, F., "Effects of Environmental and Aircraft Parameters on Wake Vortex Behavior," *Journal of Aircraft*, Vol. 51, No. 5, 2014, pp. 1490–1500. doi:10.2514/1.C032366.

[13] Daniels, T., Smith, W., and Kireev, S., "Recent Developments on Airborne Forward Looking Interferometer for the Detection of Wake Vortices," *4th AIAA Atmospheric and Space Environments Conference*, 2012, p. 2791. doi:10.2514/6.2012-2791.

[14] Michel, D. T., Dolfi-Bouteyre, A., Goular, D., Augère, B., Planchat, C., Fleury, D., Lombard, L., Valla, M., and Besson, C., "Onboard Wake Vortex Localization with a Coherent 1.5 µm Doppler LIDAR for Aircraft in Formation Flight Configuration," *Optics Express*, Vol. 28, No. 10, 2020, pp. 14374–14385. doi:10.1364/OE.377049, URL http://www.opticsexpress.org/abstract.cfm?URI=oe-28-10-14374.

[15] Hallock, J. N., and Holzäpfel, F., "A Review of Recent Wake Vortex Research for Increasing Airport Capacity," *Progress in Aerospace Sciences*, Vol. 98, 2018, pp. 27–36. doi:10.1016/j.paerosci.2018.03.003.

[16] Steen, M., and Hecker, P., "Investigating the Potential Future Usage of Combined Airborne Wake Vortex Prediction Models and Measurement Sensors," *2018 Atmospheric and Space Environments Conference*, 2018, p. 3022. doi:10.2514/6.2018-3022.

[17] Hemati, M. S., Eldredge, J. D., and Speyer, J. L., "Wake Sensing for Aircraft Formation Flight," *Journal of Guidance, Control, and Dynamics*, Vol. 37, No. 2, 2014, pp. 513–524. doi:10.2514/1.61114.

[18] DeVries, L., and Paley, D. A., "Wake Sensing and Estimation for Control of Autonomous Aircraft in Formation Flight," *Journal of Guidance, Control, and Dynamics*, 2015, pp. 1–10. doi:10.2514/1.G001138.

[19] Chichka, D. F., Speyer, J. L., Fanti, C., and Park, C. G., "Peak-Seeking Control for Drag Reduction in Formation Flight," *Journal of Guidance, Control, and Dynamics*, Vol. 29, No. 5, 2006, pp. 1221–1230. doi:10.2514/1.15424, URL https://doi.org/10.2514/1.15424.

[20] Binetti, P., Ariyur, K. B., Krstic, M., and Bernelli, F., "Formation Flight Optimization Using Extremum Seeking Feedback," *Journal of Guidance, Control, and Dynamics*, Vol. 26, No. 1, 2003, pp. 132–142. doi:10.2514/2.5024.

[21] Hanson, C. E., "A Fuzzy Technique for Performing Lateral-Axis Formation Flight Navigation Using Wingtip Vortices," 2003.

[22] Caprace, D.-G., Winckelmans, G., Chatelain, P., and Eldredge, J., "Wake Vortex Detection and Tracking for Aircraft Formation Flight," *AIAA Aviation 2019 Forum*, edited by AIAA, 2019. doi:10.2514/6.2019-3329, URL `https://arc.aiaa.org/doi/abs/10.2514/6.2019-3329`.

[23] Van Leeuwen, P. J., "Comment on "Data Assimilation Using an Ensemble Kalman Filter Technique"," *Monthly Weather Review*, Vol. 127, No. 6, 1999, pp. 1374–1377. doi:10.1175/1520-0493(1999)127<1374:CODAUA>2.0.CO;2.

[24] Chatelain, P., Curioni, A., Bergdorf, M., Rossinelli, D., Andreoni, W., and Koumoutsakos, P., "Billion Vortex Particle Direct Numerical Simulations of Aircraft Wakes," *Computer Methods in Applied Mechanics and Engineering*, Vol. 197, No. 13, 2008, pp. 1296–1304. doi:10.1016/j.cma.2007.11.016.

[25] Cottet, G.-H., and Koumoutsakos, P., *Vortex Methods, Theory and Practice*, Cambridge University Press, 2000.

[26] Caprace, D.-G., Winckelmans, G., and Chatelain, P., "An Immersed Lifting and Dragging Line Model for the Vortex Particle-Mesh Method," *Theoretical and Computational Fluid Dynamics*, Vol. 34, 2020, pp. 21–48. doi:10.1007/s00162-019-00510-1.

[27] Chatelain, P., Duponcheel, M., Caprace, D.-G., Marichal, Y., and Winckelmans, G., "Vortex Particle-Mesh Simulations of Vertical Axis Wind Turbine Flows: from the Airfoil Performance to the very Far Wake," *Wind Energy Science*, Vol. 2, No. 1, 2017, p. 317. doi:10.5194/wes-2-317-2017.

[28] Chatelain, P., Duponcheel, M., Zeoli, S., Buffin, S., Caprace, D.-G., Winckelmans, G., and Bricteux, L., "Investigation of the Effect of Inflow Turbulence on Vertical Axis Wind Turbine Wakes," *Journal of Physics: Conference Series*, Vol. 854, No. 1, 2017, p. 012011. doi:10.1088/1742-6596/854/1/012011.

[29] Caprace, D.-G., Chatelain, P., and Winckelmans, G., "Wakes of Rotorcraft in Advancing Flight: A Large Eddy Simulation Study," *Physics of Fluids*, Vol. 32, No. 8, 2020, p. 087107. doi:10.1063/5.0015162.

[30] Chatelain, P., Backaert, S., Winckelmans, G., and Kern, S., "Large Eddy Simulation of Wind Turbine Wakes," *Flow, Turbulence and Combustion*, Vol. 91, No. 3, 2013, pp. 587–605. doi:10.1007/s10494-013-9474-8.

[31] Jeanmart, H., and Winckelmans, G., "Investigation of Eddy-Viscosity Models Modified Using Discrete Filters: A Simplified Regularized Variational Multiscale Model and an Enhanced Field Model," *Physics of Fluids*, Vol. 19, No. 5, 2007, p. 055110. doi:10.1063/1.2728935.

[32] Mann, J., "Wind Field Simulation," *Probabilistic Engineering Mechanics*, Vol. 13, No. 4, 1998, pp. 269–282. doi:10.1016/S0266-8920(97)00036-2.

[33] Evensen, G., *Data Assimilation: the Ensemble Kalman Filter*, Springer Science & Business Media, 2009. doi:10.1007\%2F978-3-642-03711-5.

[34] Evensen, G., "Sequential Data Assimilation with a Nonlinear Quasi-geostrophic Model Using Monte Carlo Methods to Forecast Error Statistics," *Journal of Geophysical Research: Oceans*, Vol. 99, No. C5, 1994, pp. 10143–10162. doi:10.1029/94JC00572.

[35] Burgers, G., Jan van Leeuwen, P., and Evensen, G., "Analysis Scheme in the Ensemble Kalman Filter," *Monthly weather review*, Vol. 126, No. 6, 1998, pp. 1719–1724.

[36] Darakananda, D., Eldredge, J., da Silva, A., Colonius, T., and Williams, D. R., "EnKF-based Dynamic Estimation of Separated Flows with a Low-Order Vortex Model," *2018 AIAA Aerospace Sciences Meeting*, 2018, p. 0811. doi:10.2514/6.2018-0811.

[37] da Silva, A. F., and Colonius, T., "A Bias-aware EnKF Estimator for Aerodynamic Flows," *2018 Fluid Dynamics Conference*, 2018, p. 3225. doi:10.2514/6.2018-3225.

[38] Whitaker, J. S., and Hamill, T. M., "Evaluating Methods to Account for System Errors in Ensemble Data Assimilation," *Monthly Weather Review*, Vol. 140, No. 9, 2012, pp. 3078–3089. doi:10.1175/MWR-D-11-00276.1.

[39] Breitsamter, C., "Wake Vortex Characteristics of Transport Aircraft," *Progress in Aerospace Sciences*, Vol. 47, No. 2, 2011, pp. 89 – 134. doi:10.1016/j.paerosci.2010.09.002, URL `http://www.sciencedirect.com/science/article/pii/S0376042110000576`.

[40] Kutta, W., "Auftriebskräfte in strömenden Flüssigkeiten," *Illustrierte Aeronautische Mitteilungen*, Vol. 6, No. 133, 1902, pp. 133–135.

[41] Joukowski, N., "Sur les Tourbillons Adjoints," *Transcript of the Physical Section, Imperial Society of Friends of Natural Sciences, Moscow*, Vol. 23, 1906.

[42] Caprace, D.-G., Chatelain, P., and Winckelmans, G., "Lifting Line with Various Mollifications: Theory and Application to an Elliptical Wing," *AIAA Journal*, Vol. 57, No. 1, 2019, pp. 17–28. doi:10.2514/1.J057487.

[43] Cook, M. V., *Flight Dynamics Principles: a Linear Systems Approach to Aircraft Stability and Control*, Butterworth-Heinemann, 2012.

[44] Friedland, B., "Treatment of Bias in Recursive Filtering," *IEEE Transactions on Automatic Control*, Vol. 14, No. 4, 1969, pp. 359–367.

[45] Zanetti, R., and Bishop, R. H., "Kalman Filters with Uncompensated Biases," *Journal of Guidance, Control, and Dynamics*, Vol. 35, No. 1, 2012, pp. 327–335.

[46] De Visscher, I., "Interaction of Wake Vortices with the Atmosphere and the Ground : Advanced Numerical Simulation and Operational Modeling," Ph.D. thesis, Université catholique de Louvain, 2012.